

The Pennsylvania State University
The Graduate School
College of Engineering

**AN ATMOSPHERIC-PRESSURE MICROGAP PLASMA SOURCE FOR
OZONE GENERATION**

A Thesis in
Electrical Engineering
by
Timothy Brubaker

© 2014 Timothy Brubaker

Submitted in Partial Fulfillment
of the Requirements
for the Degree of

Master of Science

December 2014

The thesis of Timothy Brubaker was reviewed and approved* by the following:

Sven G. Bilén

Associate Professor of Engineering Design, Electrical Engineering, and
Aerospace Engineering
Thesis Advisor

Victor P. Pasko

Professor of Electrical Engineering and Graduate Program Coordinator

Sean D. Knecht

Research Associate at the Applied Research Laboratory

Kultegin Aydin

Professor of Electrical Engineering and Department Head

*Signatures are on file in the Graduate School.

Abstract

Ozone is a powerful oxidant commonly used to remove pollutants in water. Although widely implemented, conventional ozone generators create corona or glow discharges in the air using high-voltage power supplies that present a hazard for those working on or around the devices. In this thesis, we investigate the use of microplasmas to create a low-voltage ozone generator.

This thesis presents the design and preliminary characterization of a resonant-cavity microplasma source operating at 2.45 GHz. Microwave-excited microplasmas have been shown to create stable, non-equilibrium plasmas at atmospheric pressure. These plasmas do not require high voltages, vacuum systems, or noble gases, making them an attractive alternative for generating air plasmas. This particular design uses a resonant cavity to create a discharge across two knife-edge electrodes, separated by a $\approx 100\text{-}\mu\text{m}$ gap.

A plasma was established across the gap using a hand-held Tesla coil. The plasma spanned 14 mm at 116-W applied power and generated ozone at 0.002 %wt. Through spectral analysis, we found that the N_2 first-positive and second-positive systems and the N_2^+ first negative systems dominate the plasma. We also identify the reactive species OH, NO, and O, which might find applications outside of water treatment.

A brief overview of laser-based diagnostics that would aid in characterizing microplasma sources will also be presented, along with specifications for laser-induced fluorescence and laser scattering systems. Lastly, we explore the potential benefits and shortcomings of the source design and recommendations for future research using microplasma sources of similar design.

Table of Contents

List of Figures	vi
List of Tables	viii
List of Symbols	ix
Acknowledgments	xi
Chapter 1	
Introduction	1
1.1 Motivation	1
1.2 Contributions	2
1.3 Thesis Organization	2
Chapter 2	
Background	3
2.1 Introduction to Microplasmas and Their Applications	3
2.1.1 Types of Microplasmas	3
2.1.1.1 Microgaps	3
2.1.1.2 Microcavities	4
2.1.1.3 Microtorches	5
2.1.2 Applications of Microplasmas	5
2.1.2.1 Water and Gas Treatment	5
2.1.2.2 Plasmas for Health Care	5
2.1.2.3 Materials Processing	6
2.2 Microgap Plasmas at Atmospheric Pressure	6
2.2.1 Discharge Theory	6
2.2.2 Gas Chemistry	10
2.2.2.1 The Prevalence of Argon and Helium in Plasma Systems	10
2.2.2.2 Air Chemistry and Ozone Production	11
2.3 Optical Emission Spectroscopy	11
2.3.1 Emission Spectra Fundamentals	12
2.3.2 Deriving Temperature from Emissions	12

Chapter 3	
Design of a Microwave Microgap Plasma Source	15
3.1 Design Summary and Assumptions	15
3.2 Microwave Theory and Discharge Requirements	16
3.2.1 Breakdown Electric Field	16
3.2.2 Transmission Line Model	17
3.3 Electric Field Distribution of the Plasma Source	18
3.4 Physical Model and Tuning	21
3.4.1 Razor Blade Electrodes	21
3.4.2 PCB Electrodes	22
3.4.3 Reflection Coefficient	23
3.4.4 Ignition and Maintenance Power Testing	24
3.5 Previous Designs	27
Chapter 4	
Results	32
4.1 Emission Spectrum: Observations and Analysis	32
4.2 Gas Production and Thermal Properties	32
Chapter 5	
Improving Plasma Diagnostics Capabilities	35
5.1 Laser Diagnostics and Scattering Theory	35
5.1.1 Laser Induced Fluorescence	35
5.1.2 Rayleigh, Raman, and Thomson Scattering	37
5.2 Preliminary Design of a Laser Scattering System	39
5.2.1 Laser Selection	39
5.2.2 Laboratory Setup and Electronics	40
Chapter 6	
Conclusions and Future Work	42
Appendix A	
COMSOL Multiphysics Notes	43
A.1 Materials	43
A.2 Port Excitation	43
A.3 Meshing	43
A.4 Parametric Sweeps	43
A.5 Solving and Plotting	44
Appendix B	
Plasma Source Drawings	45
Appendix C	
LabVIEW VI for Data Acquisition	50
Appendix D	
LTS Calculator	51
Bibliography	53

List of Figures

2.1	Examples of microwave microgap resonators that use standing waves to cause breakdown.	4
2.2	Illustration of EII and SEE processes occurring between DC-biased parallel plate electrodes.	6
2.3	Paschen curve for a 1-mm microgap discharge in air using Equation 2.6.	8
2.4	Frequency response of the breakdown voltage in microgaps.	9
2.5	Microwave Paschen curves for a microwave split-ring resonator.	10
2.6	Potential curves of N_2 , N_2^+	13
2.7	First positive, first negative, and second positive systems of nitrogen	14
3.1	Drawing of the microwave microplasma source.	16
3.2	Transmission line model for the plasma source.	17
3.3	Dimensions and electric field distribution for a TEM mode parallel plate transmission line.	18
3.4	Wire frame model of the microwave microplasma source. Only the center conductor and dielectric of the SMA connector were modeled.	19
3.5	Front view of the plasma source electric field simulation at 1 W.	20
3.6	Side view of the plasma source electric field simulation at 1 W.	20
3.7	Side view of the microgap electric field simulation at 1 W. The high electric fields extend outward, but are strongest within the gap.	21
3.8	Electric field streamline cartoons for the front and side views of the plasma source. The cartoons were drawn from simulation results.	22
3.9	Magnetic field streamline cartoon for the top view of the plasma source. Two local maxima are found near the edges of the electrodes. The cartoon was drawn from simulation results.	23
3.10	3D and drawing views of the plasma source with major dimensions.	24
3.11	Photographs of the assembled microplasma source.	25
3.12	Flex PCB electrode design. A microgap is micromachined out of a copper-clad circuit board, providing better uniformity than hand-positioning electrodes. . . .	26
3.13	S_{11} of plasma source from 2–3 GHz using stainless steel razor blades.	26
3.14	Power and spectral measurements setup.	28
3.15	Plasma source after sputtering has removed material.	29
3.16	Plasma volume using copper electrodes and 116-W applied power.	29
3.17	The microstrip plasma source using electrodes made from 1/32 in copper sheet. .	30
3.18	Microplasma from the re-created source at varying applied power.	30
3.19	Preliminary source design with tunable short and razor blade electrodes.	31

3.20	Microplasma from the preliminary design using copper electrodes and stainless steel razor blades.	31
4.1	Normalized microplasma spectrum from 200–1000 nm.	33
4.2	Ozone test configuration and chamber during operation.	34
5.1	The fluorescence process.	36
5.2	Schematic for a single-species LIF system.	37
5.3	Rayleigh and Raman scattering processes.	38
5.4	Schematic for a Thomson and Raman scattering system.	40
B.1	Bottom plate of plasma source.	45
B.2	Top plate of plasma source.	46
B.3	Back plate of plasma source.	47
B.4	Shorting block for tuning.	48
B.5	Assembled plasma source.	49
C.1	Front panel of data acquisition VI.	50
C.2	Block diagram of data acquisition VI.	50
D.1	Excel calculator for finding LTS system SNR based on instrumentation and plasma parameters.	52

List of Tables

2.1	Ozone Production and Destruction Processes in Dry Air Plasmas	11
3.1	Breakdown Electric Field Parameters	17
5.1	LIF Parameters for Common Reactive Plasma Species	36
5.2	Types of Scattering and Derived Plasma Parameters	38

List of Symbols

α	First Townsend ionization coefficient, number of ionizations, p. 7
Δt	Pulse and gating duration, s, p. 39
ϵ	Permittivity, $\text{F}\cdot\text{m}^{-1}$, p. 18
γ	Second Townsend ionization coefficient, the ratio of emitted electrons to incident ions, p. 7
γ_r	Recombination rate, s^{-1} , p. 8
λ	Laser wavelength, m, p. 38
λ_D	Plasma Debye length, m, p. 38
μ_{bd}	Breakdown parameter, unitless, p. 7
μ	Permeability, $\text{H}\cdot\text{m}^{-1}$, p. 18
Ω_s	Collection optics solid angle, sr, p. 39
θ	Scattering angle, degrees, p. 39
ν_c	Collision frequency, s^{-1} , p. 9
A	Gas constant, $\text{Torr}^{-1}\cdot\text{m}^{-1}$, p. 7
B	Gas constant, $\text{V}\cdot\text{Torr}^{-1}\text{m}^{-1}$, p. 7
c	Speed of light, $\text{m}\cdot\text{s}^{-1}$, p. 39
C	Bremsstrahlung factor, unitless, p. 39
d	Gap distance between electrodes, m, p. 7
d_l	Laser beam diameter, m, p. 39
D	Diffusion Coefficient, $\text{m}^2\cdot\text{s}^{-1}$, p. 8
E	Electric field, $\text{V}\cdot\text{m}^{-1}$, p. 7
E_{bd}	Breakdown electric field, $\text{V}\cdot\text{m}^{-1}$, p. 7

f_0	Center frequency of resonant cavity, Hz, p. 24
f_{lower}	Frequency below f_0 that is 3 dB down, Hz, p. 24
f_{upper}	Frequency above f_0 that is 3 dB down, Hz, p. 24
f_{cr}	Critical frequency between microgap operating regimes, Hz, p. 9
h_p	Planck's constant, $\text{m}^2\cdot\text{kg}\cdot\text{s}^{-1}$, p. 39
h	Height of parallel plate, m, p. 18
L_c	Optics distance from the scattering volume, m, p. 39
L_s	Length of scattering volume, m, p. 39
m_e	Mass of electron, kg, p. 9
N_i	Number of incident laser photons, p. 39
P	Gas pressure, Torr (mm Hg), p. 7
Q	Quality factor, unitless, p. 23
Q_e	Product of the optical transmission and detector quantum efficiencies, unitless, p. 39
r_e	Classical electron radius, m, p. 39
T_e	Electron temperature, K, p. 39
V	Voltage, V, p. 7
w	Width of parallel plate, m, p. 18
Z	Impedance, Ω , p. 18
Z_{eff}	Effective ion charge, unitless, p. 39

Acknowledgments

I'd like to first acknowledge my advisor, Dr. Sven Bilén, and Dr. Sean Knecht for their support and guiding questions during this research. I also thank Dr. Victor Pasko for serving on my committee. I have also been helped countless times by my labmates and want to extend a large thank you to Jesse McTernan for letting me bounce ideas around and instructing me on the finer points of machining, as well as to the SSPL students that provide so much comic relief.

Chapter 1 |

Introduction

Plasma-based devices are an important technology in infrastructure and consumer markets. We can point to neon lights and street lamps as examples of widely-adopted plasma devices. However, just as we would describe both diamond and copper as solids, there are many types of plasmas with vastly different properties and, thus, they find use in different applications. Indeed, plasmas are also found in materials processing, biomedicine, machining, and space systems, where plasma can be hot enough to melt meteoroids or cold enough to apply to our skin.

Microplasmas are a subset of plasmas that are spatially confined to within one millimeter in one or more dimensions that have seen a significant increase in research over the past 15 years [1]. These plasmas offer novel operation schemes and applications, including low-power microwave plasmas at atmospheric pressure. This work presents a microwave plasma source using a microgap discharge for operation in atmospheric-pressure air.

1.1 Motivation

Ozone (O_3), discovered over 150 years ago, has found use as a disinfectant in several commercial and residential settings such as water treatment facilities and hot tubs. Ozone not only oxidizes pollutants, but can also alter the taste, color, odor, and other properties of drinking water [2]. A conventional ozone generator, sometimes called an “ozonator”, uses an electrical discharge to dissociate diatomic oxygen (O_2) into atomic oxygen (O) atoms that bond with O_2 to form ozone. These devices typically use high-voltage AC power (≥ 1 kV) and produce 1–4 %wt ozone when fed with air [2]. We seek an alternative solution that removes high voltages and reduces the size, weight, and power requirements. In an effort to make a man-portable, low-power ozone source with similar or better ozone production efficiency, we will answer the following questions: (1) “Can microwave, microgap plasmas offer an efficient, low-voltage ozone generator?” and (2), “Can we scale the plasma device, either as a single source or in an array?”

1.2 Contributions

This thesis covers the design and testing of a microwave microgap plasma source for ozone generation. The source is designed for low-power operation at atmospheric pressures and does not require high-voltage power supplies. A one-dimensional array or “line” of microplasma could be created by lining up these sources, which would provide a larger plasma volume for increased ozone production. A second part of this thesis will introduce the motivation and preliminary designs for laser-based diagnostics that would expand Penn State’s capabilities to investigate microplasmas.

1.3 Thesis Organization

This thesis first covers an introduction to microplasmas, their applications, and the diagnostics commonly used to observe them in Chapter 2. Chapter 3 then applies these concepts to cover the design and preliminary characterization of the plasma source. Plasma spectral analysis and ozone production are discussed in Chapter 4. Chapter 5 then departs from the plasma source design to discuss laser-based diagnostics to better characterize such a source. Chapter 6 presents the conclusions and future work.

Chapter 2 |

Background

This chapter reviews existing theory and experimental material relevant to microgap plasmas in order to establish a framework for this research. Background on laser diagnostics are covered in Chapter 5 to remain fresh in the reader's mind during the relevant sections.

2.1 Introduction to Microplasmas and Their Applications

A microplasma refers to a plasma spatially confined to within one millimeter in one or more dimensions [1]. The broad definition of microplasmas leads to several types of plasma sources that may range several orders of magnitude in size and be powered by RF, nanosecond pulsing, microwave, or DC power.

2.1.1 Types of Microplasmas

2.1.1.1 Microgaps

A microgap plasma is any plasma confined within two electrodes separated by less than 1 mm. The electrodes may have a large surface area, such as two discs separated by a small distance, or be knife-edged, such as printed circuit board traces and razor blades. Designs include, but are not limited to, the split-ring resonator [3–7], coaxial gap [8], and resonant cavity [9–11]. Three microwave resonator designs are shown in Figure 2.1. The split-ring and linear resonator designs are created on a printed circuit board (PCB) with copper trace. The third design is a parallel-plate resonant cavity that is the focus of this thesis. Resonator designs create a standing wave that, with each successive cycle of microwave power, grows in magnitude until a sufficiently high electric field causes spontaneous breakdown within the gap. This breakdown phenomenon is discussed in Section 2.2.1.

These microgap plasmas are not in local thermodynamic equilibrium and are known as non-equilibrium plasmas. This means that the electrons, ions, and neutral particles are not the same temperature, in contrast to an equilibrium plasma that has approximately the same rotational, vibrational, electronic, and electron temperatures. As a consequence, the gas temperature will be lower than the electron temperature. However, we can expect significant gas heating due

to the high collision rate between the free electrons and massive particles in microwave-excited atmospheric-pressure plasmas. We therefore will see heat transfer from the plasma to the plasma source, which will be accounted for when designing the source in Chapter 3. The gas temperatures (rotational and vibrational) of these sources are typically between 500–5000 K [10–13].

In this work, we are interested in resonant cavity designs operating at microwave frequencies (typically 2.45 GHz), which offer several benefits over DC and RF discharges. As the excitation frequency is increased, the electrons continue to follow the oscillations of the time-varying electric field but the ions are only affected by the local average values of the electric field. This results in smaller space-charge sheaths and, thus, fewer collisions between energetic particles and the electrodes. These collisions cause sputtering, the removal of particles from the electrodes surface, which lowers the electrode lifetime and changes the plasma composition.

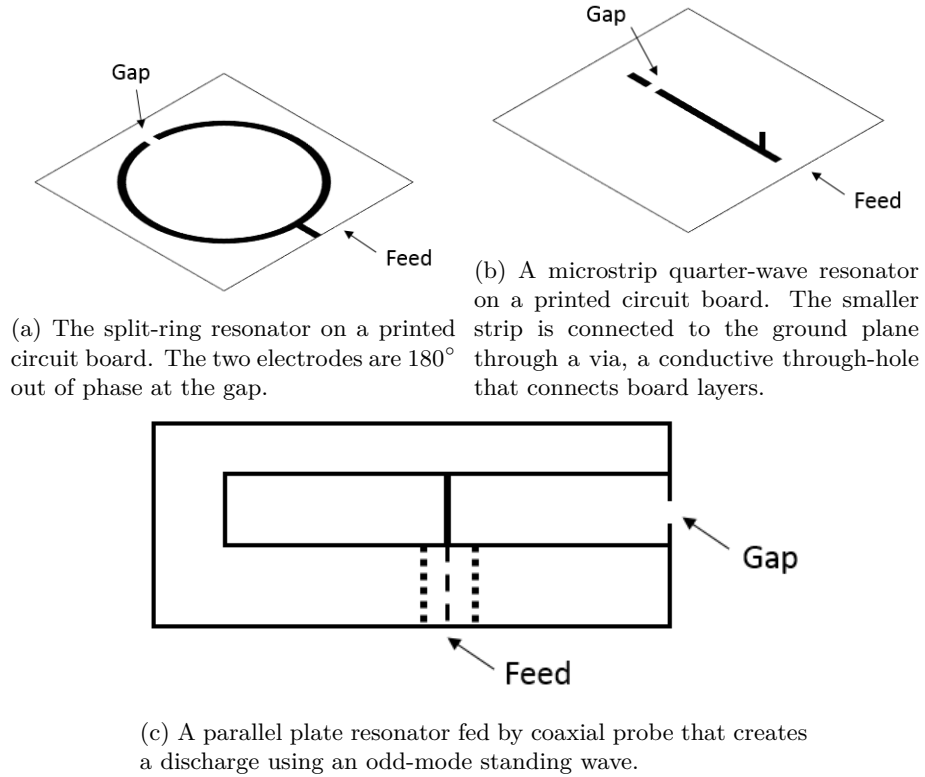


Figure 2.1: Examples of microwave microgap resonators that use standing waves to cause breakdown.

2.1.1.2 Microcavities

Microcavity plasmas are similar in construction to microelectromechanical (MEMS) devices. The microcavities are often placed in two-dimensional arrays to produce a “sheet” of plasma. Microcavity plasmas are also non-equilibrium; however, unlike the microwave-driven microgap plasma, the ions and neutral particles remain at a low temperature (~ 300 K). Therefore, the plasma can

not only provide a large, uniform surface of plasma, but also be used in temperature-sensitive applications. These plasmas are commonly used to generate light and have been commercialized for the movie-making industry as flood lights (e.g., by Eden Park Illumination) or to create ultraviolet light for experiments [1, 14].

2.1.1.3 Microtorches

Small plasma torches can go by several names, including microtorches, plasma pens/pencils, and plasma needles. Microtorches create a jet of ionized gas by pushing the gas through a tube containing a discharge. Torches, pens, and pencils are typically gap discharges, while plasma needles are small wires that cause a corona discharge at the tip. The plasma plume is at low temperature and, therefore, microtorches have found use in plasma health care. Further information on health care applications is covered in Section 2.1.2.2.

2.1.2 Applications of Microplasmas

2.1.2.1 Water and Gas Treatment

Contained plasmas that generate UV light have been commercially employed for sterilizing water. In this application, the plasma does not have direct contact with the water. Instead, the plasma acts a UV lamp. Another use of plasma is the detoxification of air and water using reactive species. Challenges with treating air and water include building a source that operates at atmospheric pressure or underwater that also allows for fluid flow past the device.

Ozone treatment of potable water and elimination of toxic vapors are two beneficial applications. However, ozone output beyond $90 \text{ g} \cdot \text{O}_3 \cdot \text{kWh}^{-1}$ (0.5–2.0 %wt) using air remains a challenge and typically uses high-voltage supplies, often operating at several kilowatts [15, 16]. Note that ozone, in general, is a poor air purifier due to slow reactions with common chemicals and the creation of irritating byproducts, but the generated ozone can be bubbled into water for treatment [17–21]. Although the water is treated with ozone, the primary oxidizer of pollutants is the hydroxyl radical (OH^*) that is formed from the dissociation of ozone.

2.1.2.2 Plasmas for Health Care

Over the past decade, plasmas for health care has emerged with promising developments in hygiene and skin cell treatments. Originally used as an antibacterial for equipment, low-temperature atmospheric plasma sources are now being applied directly to living tissue. The field is populated by many dielectric barrier discharge (DBD) plasmas, plasma torches and needles, and microplasma arrays, although it is not constrained to microplasmas.

Several processes occur during the application of a plasma to living cells: emission of ultraviolet (UV) light, creation of reactive species such as ozone, and the flow of electric currents. Plasma is, therefore, an effective sterilizer and has been applied to human skin [22], malignant cells [23], fruits [24], and fungus on wood [25]. It has been shown that increasing the intensity, oxygen content, and duration of treatment induces apoptosis and DNA damage such as double-strand

breaks [26–29]; however, plasma medicine has the potential to improve several areas of health care, including open wound treatment, cancer treatment, and surgery.

2.1.2.3 Materials Processing

Plasma processing is a blanket term that encompasses cleaning, etching, activation, and other material processing techniques. Reactive species, notably oxygen, can change the surface features of a material to make it more suitable for adhesion, hydrogen bonding, and material deposition. Plasma can also be used for silicon etching and carbon nanofabrication. Atmospheric-pressure plasmas are beneficial in this industry because they do not require costly vacuum systems.

2.2 Microgap Plasmas at Atmospheric Pressure

This section covers the necessary background to understand microgap discharges and their characteristics at standard temperature and pressure, the nominal operating conditions of the plasma source presented in this thesis.

2.2.1 Discharge Theory

We first consider a microgap with a DC (time invariant) electric field. A DC microgap plasma is created through three main processes [30]: electron impact ionization (EII), secondary electron emission (SEE), and field emission (FE). The FE mechanism is only relevant for microgaps of small distances, on order of $7\text{ }\mu\text{m}$ and smaller, because of its dependence on electron tunneling and can be neglected for our purposes [30]. A discharge dominated by the EII and SEE processes is commonly known as a Townsend discharge. Figure 2.2 provides a visual interpretation of Townsend discharges for use in the following discussion.

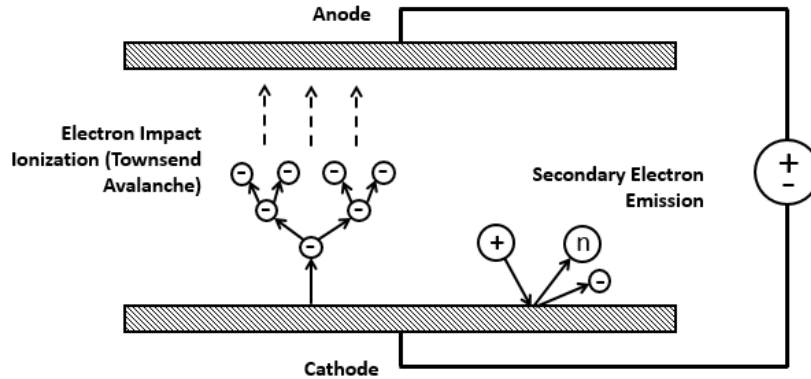


Figure 2.2: Illustration of EII and SEE processes occurring between DC-biased parallel plate electrodes.

The plasma is ignited through the application of a large electric field that causes EII. The electric field accelerates free electrons within and surrounding the microgap, giving sufficient

energy to cause the gas reaction given by



where A is a neutral particle ionized through electron impact. Double and triple reactions are also possible given a sufficient electron energy. The resulting two free electrons involved in the initial reaction are accelerated by the electric field and cause further EII. With a sufficient electric field, the number of electrons and ions continues to multiply to form the avalanche from the cathode to the anode of the source. EII is characterized by the number of ionizations, α , making it known as an α -process. This coefficient is known as the first Townsend ionization coefficient and is found via

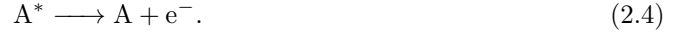
$$\alpha = APe^{(-BP/E)}, \quad (2.2)$$

where P is the gas pressure and E is the applied electric field. The equation is found in terms of applied voltage and gap distance in Semnani et al. [30], using the simple substitution $V = Ed$. Constants A and B are gas-related values and are not to be confused with a and b , the more common van der Waal's constants.

In SEE, ionized and metastable particles [31] created through EII collide with the electrode surfaces and cause additional electron emissions. The cathode's electrons absorb energy from the recombination occurring at the cathode surface and are emitted if the incident ions or metastable neutral particles impart enough energy to overcome the work function of the cathode material. There are two primary reactions for this process:



and



Similar to EII, SEE is characterized by γ , the mean ratio of emitted electrons to incident ions [32] known as the secondary ionization coefficient (or Townsend's second ionization coefficient), and is called a γ -process. The coefficient is found through the equation

$$\mu_{bd} = \gamma \exp \left(\int_0^d \alpha(x') dx' - 1 \right). \quad (2.5)$$

Here, μ_{bd} is the breakdown parameter and d is the gap distance. The breakdown threshold occurs at $\mu_{bd} = 1$, and breakdown occurs for values of $\mu_{bd} \geq 1$.

The combination of the two processes, assuming $\mu_{bd} = 1$, yields the Paschen Law for gap distance d [30],

$$E_{bd} = \frac{BP}{\ln(Pd) + \ln \left[\frac{A}{\ln(1/\gamma+1)} \right]}. \quad (2.6)$$

This equation was set forth by F. Paschen in his 1889 paper [33] to determine breakdown voltages, and leads to the well-known Paschen curves that describe how the breakdown voltage is dependent

on the pressure and distance term Pd . An example curve is shown in Figure 2.3.

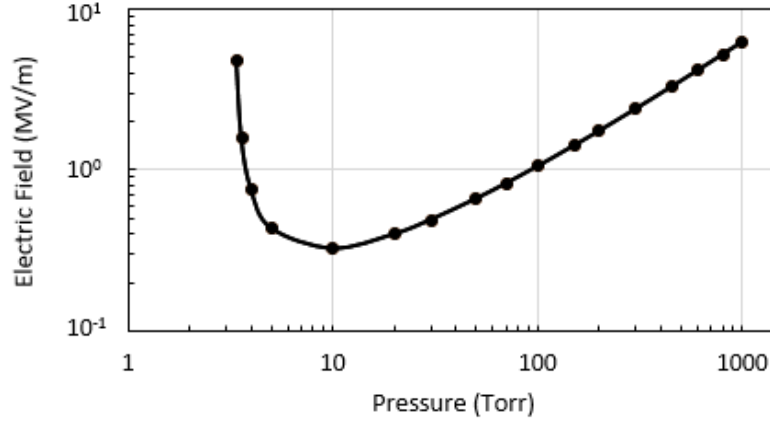


Figure 2.3: Paschen curve for a 1-mm microgap discharge in air using Equation 2.6.

It was found that discharges occurred outside of small gaps and within larger gaps [30]. This was investigated because discharges occurred at lower breakdown voltages than expected for small gaps. The path of the discharge, then, may not be a direct line between the electrodes. This effect has not yet been quantitatively explained and will be omitted from the source design presented in this thesis.

We now extend the discharge discussion to include the frequency response of the breakdown electric field. There have been several semi-empirical models for describing microwave breakdown in free space and within parallel-plate waveguides [34–38]. In brief, the threshold or breakdown electric field occurs when the ionization and recombination rates are equal, which may be expressed as

$$\nu_i(P, E_{bd}) - \gamma_r(P) = 0, \quad (2.7)$$

where ν_i is the ionization rate and γ_r is the recombination rate. Here,

$$\gamma_r = \left(\frac{m\pi}{d}\right)^2 D, \quad (2.8)$$

and

$$D = \left(29 + 0.9 \frac{E_{bd}}{P}\right) \cdot 10^4 P, \quad (2.9)$$

where $m = 0, 1, 2, \dots$ and D is the diffusion coefficient defined by MacDonald et al. [38]. This microwave model has shown good agreement with gaps on order of a centimeter operating at low pressure; however, the model is not valid for small gap sizes at atmospheric pressure, where Equations 2.7–2.9 yield high breakdown electric fields that are in disagreement with recent microgap literature [5, 39].

Semnani et al. [39] have shown, through particle-in-cell simulation, that the breakdown electric field for microwave microgaps has three primary regimes: the boundary, diffusion, and inertia

controlled regimes. The typical DC and low-frequency RF microgap operates within the boundary controlled regime, where there is significant interaction between charged particles and the device walls. There, the Paschen model provides a relatively accurate prediction of the breakdown electric field.

As the frequency is increased, we reach a critical frequency that marks the transition between the boundary-controlled and diffusion-controlled regimes. Above this critical frequency, the Paschen model is no longer an accurate predictor because the excitation frequency is higher than the collision frequency of the particles. In this case, electrons are not collected by the anode and, therefore, EII occurs more often, leading to a lower breakdown electric field. In this diffusion-controlled regime, the breakdown voltage was found to be about three times lower than in the boundary-controlled regime. The simulation was then plotted against experimental data, seen in Figure 2.4, and shows good agreement. The reduction in breakdown electric field is similar to experimental observations made by Iza and Hopwood [5], who have taken measurements of a split-ring resonator operating in air and argon. The split-ring resonator's experimental Paschen curves are shown in Figure 2.5, with the theoretical DC Paschen curve plotted for reference.

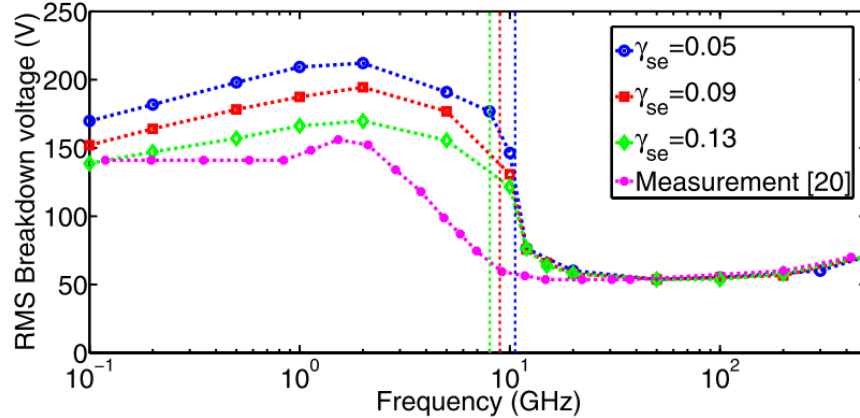


Figure 2.4: Comparison of simulated and measured frequency response of breakdown voltage and the predicted critical frequency points in a 15 μm argon gap with nickel electrodes [39].

The breakdown electric field within the boundary controlled regime is used to find the critical frequency through the expression

$$f_{\text{cr}} = \frac{eE}{\sqrt{2}\pi m_e \nu_c d}, \quad (2.10)$$

where e is the fundamental unit of charge, m_e is the mass of an electron, and ν_c is the collision frequency [39]. There is not yet an analytical model for estimating the required breakdown electric field, but we will use the critical frequency expression to determine our operating regime in Chapter 3.

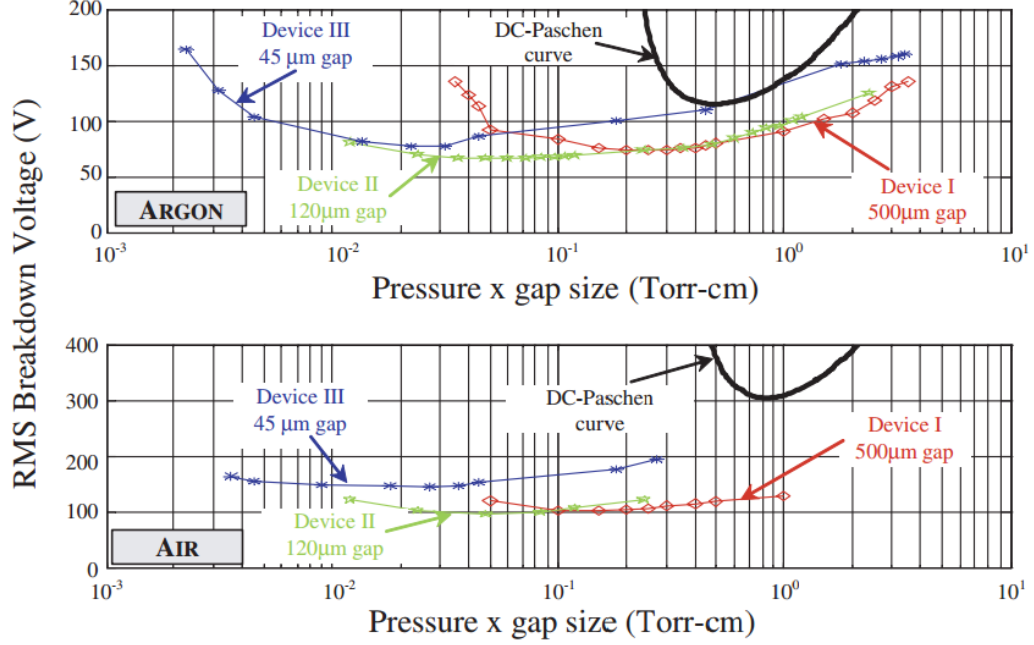


Figure 2.5: Microwave breakdown curves for a microwave split-ring resonator plotted against a theoretical DC breakdown using Paschen theory [5].

2.2.2 Gas Chemistry

Of particular importance in plasma analysis is the collisional radiative model (CRM), a model of all the significant particle-particle and particle-wall interactions of a system. As shown later, the choice of gas will heavily influence the complexity and feasibility of creating a CRM. In addition to modeling benefits, the choice of gas and pressure can also impact plasma source design requirements.

2.2.2.1 The Prevalence of Argon and Helium in Plasma Systems

The noble gases argon and helium have been used in an abundance of plasma literature. The use of a single or dominant gas in plasma systems leads to simplified gas chemistry and, therefore, more predictable results, meaning system performance and anomalies are more easily characterized. Furthermore, lower-power systems can be used because the breakdown voltage of argon and helium is lower than that of air. Because of its simplicity, a plasma system using pure argon can be simulated using commercial packages such as COMSOL Multiphysics. These software packages often provide examples using argon as a starting point.

Because we are interested in self-ignition in the air, this work has fore-gone the use of noble gases. Similar designs by Gregorio and Kono [10,11] have been extensively studied in argon.

Table 2.1: Ozone Production and Destruction Processes in Dry Air Plasmas [42–45]

Reaction Mechanism
$e^- + O_2 \longrightarrow O + O + e^-$
$e^- + N_2 \longrightarrow N + N + e^-$
$O + O_2 + M \longrightarrow O_3 + M$
$O + O + M \longrightarrow O_2 + M$
$N + O_2 \longrightarrow NO + O$
$N + O_3 \longrightarrow NO + O_2$
$O + NO_2 \longrightarrow NO + O_2$
$NO + O_3 \longrightarrow NO_2 + O_2$
$NO_2 + O_3 \longrightarrow NO_3 + O_2$
$NO_2 + NO_3 \longrightarrow N_2O_5$
$NO + NO_3 \longrightarrow NO_2 + NO_2$
$N_2O_5 \longrightarrow NO_2 + NO_3$
$O + N_2O_5 \longrightarrow NO_2 + NO_2 + O_2$
$NO_2 + O_3 \longrightarrow NO_3 + O_2$
$O + NO_3 \longrightarrow O_2 + NO_2$

2.2.2.2 Air Chemistry and Ozone Production

It is a perhaps daunting challenge to incorporate the many chemical reactions of air into a plasma system model. Only including the most significant reactions between nitrogen and oxygen leads to 15 species [40], while more-complete air systems may have over 75 species and almost 500 reactions [41]. Comprehensive models are possible using numerical code such as NEQAIR (nonequilibrium air radiation), a line-by-line code developed by NASA for simulating an emission spectrum that calculates the spontaneous emission, stimulated emission, and absorption due to the modeled species. Alternatively, researchers may develop code unique to their application.

In this thesis, we are specifically interested in the production of ozone. In dry air plasmas, ozone is primarily produced through the reactions given in Table 2.1, where M is diatomic oxygen or nitrogen. Note that Table 2.1 does not include reactions with excited particles, for example



A more complete list of reactions consisting of 17 species is provided by Kitayama and Kuzumoto [42]. Many commercial ozone generators use pure oxygen feeds because the nitrogen in air reacts with the ozone to produce nitrogen oxides (NO_x), thereby decreasing the efficiency of the generator.

2.3 Optical Emission Spectroscopy

Optical Emission Spectroscopy (OES) is a passive optical diagnostic for characterizing plasma systems. When the excited particles within a plasma relax to lower energy levels, energy is released as photons whose wavelength is dependent upon the transition. Therefore, if we were to measure the light given off by the plasma system, it is possible to determine which bound-electron

transitions occurred and how often. This is the principle behind OES.

OES is non-intrusive and can provide several gas parameters, including electron temperature, population density of heavy particle states, and gas temperature. OES uses a simpler hardware setup than laser systems and, unlike *in situ* diagnostics, does not affect the system under test.

2.3.1 Emission Spectra Fundamentals

A common characteristic of air plasmas is visible light emissions from diatomic nitrogen (N_2). Therefore, we will use the nitrogen to illustrate the emission behavior of plasma systems. Figure 2.6 is a partial diagram of the potential curves of N_2 , N_2^+ . Several additional curves exist [46,47], but are outside the scope of this thesis. Along each curve are the available vibrational and rotational states that the particle may occupy. These available states lead to a collection of possible transitions when the particle decays from an excited state, many of which emit photons outside of the visible spectrum. We will focus on the most common transitions in the visible region, which have been grouped into transition systems.

There are three nitrogen systems of note within the visible spectrum: (1) The $C^3\Pi_u - B^3\Pi_g$ second positive system (SPS) of N_2 spanning 2680–5460 Å, (2) the $B^3\Pi_g - A^3\Sigma_u^+$ first positive system (FPS) of N_2 spanning 4780–25310 Å, and (3) the $B^2\Sigma_u^+ - X^2\Sigma_g^+$ first negative system of N_2^+ spanning 2860–5870 Å. These three transitions are illustrated in Figure 2.7, a simplified diagram of the nitrogen potential curves. The nomenclature for these systems originated from where they were observed within a column of nitrogen plasma, that is, the positive and negative systems consist of the emissions that were seen in the positive and negative columns.

2.3.2 Deriving Temperature from Emissions

There are several nitrogen “thermometer” techniques for determining gas temperature in atmospheric air plasmas. The rotational temperature historically has been estimated by a variety of curve fitting and line-ratio techniques that use the nitrogen second-positive [49–51], first-positive [52], and first negative-systems [49]. The rotational temperature is a reasonable indicator of the gas temperature because of fast relaxation times and small differences in energy between rotational levels [53]. Methods for finding the vibrational temperature often use numerical simulation to fit the experimental spectrum. A full spectral simulation requires a comprehensive CRM for nitrogen, which has been referred to as a nitrogen kinetic model [54].

More recently, trace gases have also been used to measure the electron temperature of the system. Trace rare gases optical emission spectroscopy introduces small concentrations of Ne, Ar, Kr, or Xe into a plasma system and determines the temperature based on the simpler noble gas transitions [54]. For further information, Zhu et al. 2010 [54] provides a thorough treatment on existing OES techniques.

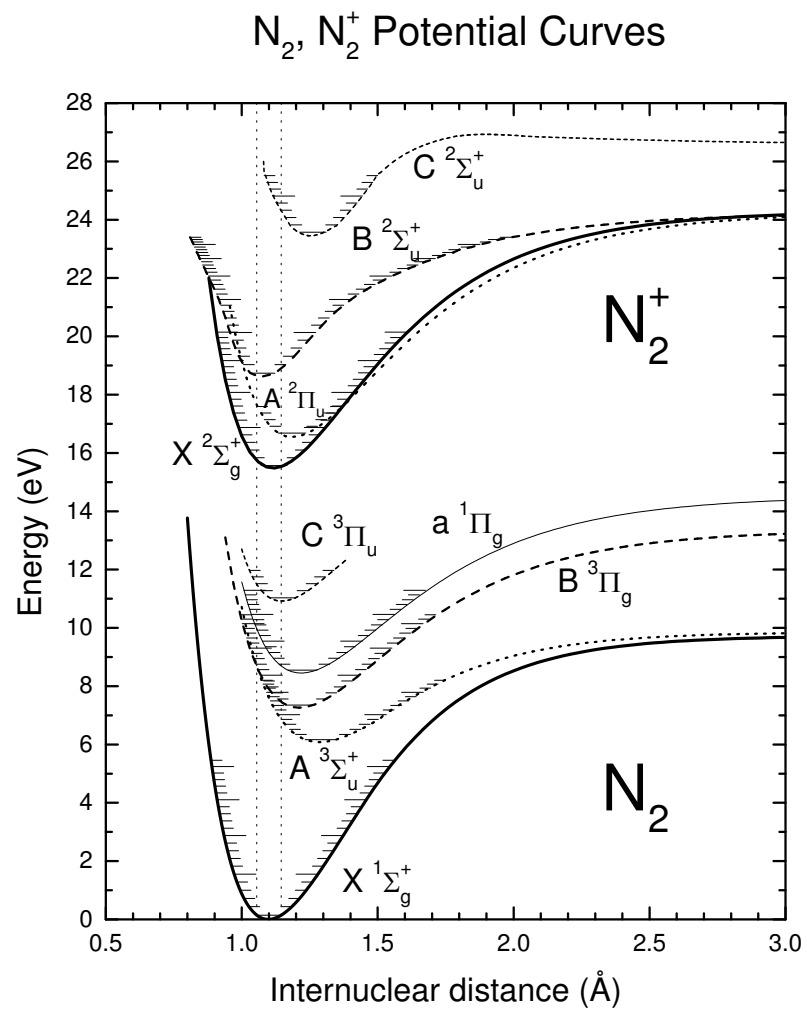


Figure 2.6: Potential Curves of N_2, N_2^+ [48]

Dominant Nitrogen Transitions

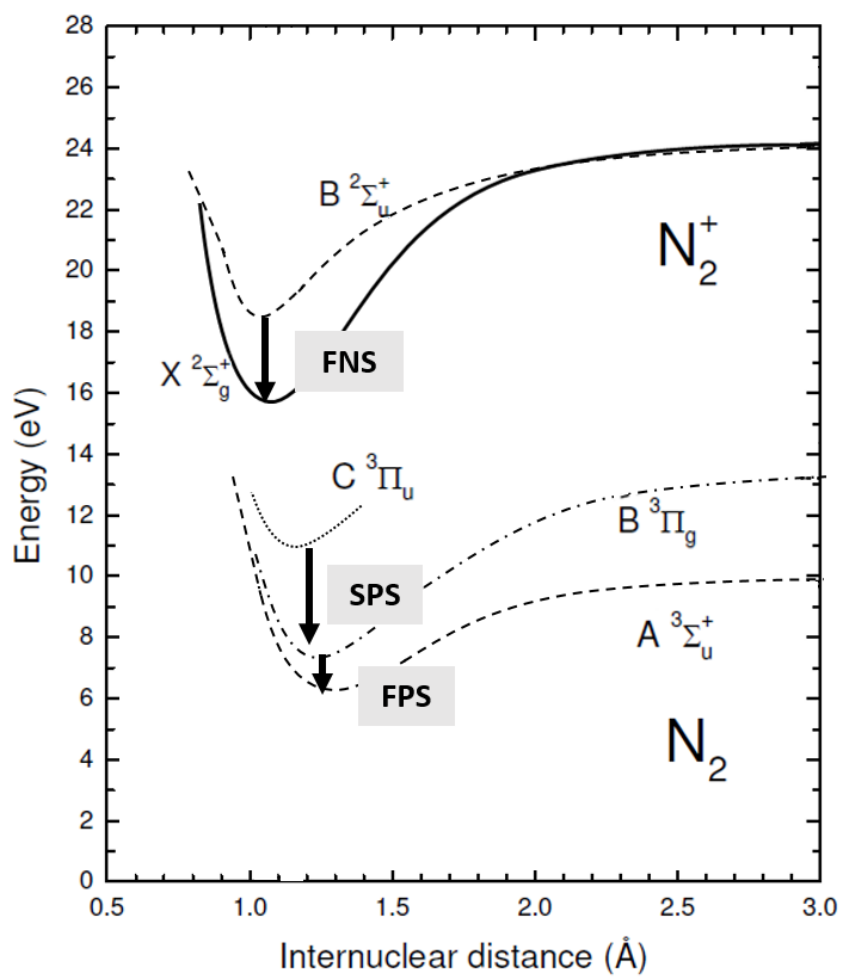


Figure 2.7: First positive, first negative, and second positive systems of nitrogen

Chapter 3 |

Design of a Microwave Micro-gap Plasma Source

This chapter covers the design, simulation, and construction of the microwave microgap plasma source for ozone generation.

3.1 Design Summary and Assumptions

The plasma source, shown in Figure 3.1, is a parallel-plate resonant cavity fed by a coaxial probe. The design of this plasma source was heavily influenced by previous work by Kono et al. [10], which had a similar coaxial-to-waveguide structure. To move toward man-portable devices, the structure was adopted but modified to work with low-power coaxial feeds instead of the cyclotron waveguide feed originally used. The same gap width of $100\text{ }\mu\text{m}$ was chosen, but was an otherwise arbitrary decision. A second group has looked at miniaturizing the same design [11], but has decreased the gap length and added a wide ground plane, thus making it less applicable to our plasma line concept.

The source is fed microwave power from a $50\text{-}\Omega$ coaxial cable at a frequency of 2.45 GHz . Before ignition of the plasma, the device appears as an open circuit and thus the impedance, Z_p , is infinite. However, due to the conductivity of the plasma within the microgap, it appears as a finite load during operation. We, therefore, have two cases to design for: (1) $Z_p \rightarrow \infty$ and (2) Z_p finite, but small. A larger electric field is required for ignition than for sustaining the plasma. Matching the open circuit condition will result in a lower amount of power applied to ignite the plasma, but leads to inefficiencies when operating the plasma because the load impedance changes after breakdown. Since the operation time is expected to be significantly longer than ignition, we would ideally match for the second condition if we want to minimize the total energy consumption. Instead, we will match for the open-circuit condition to limit the maximum power.

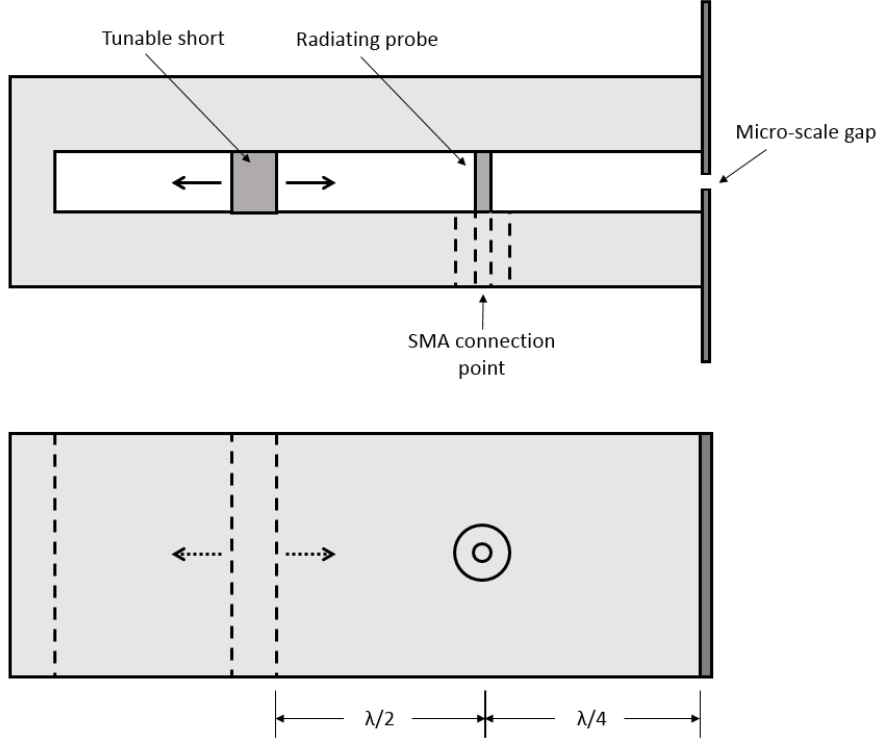


Figure 3.1: Drawing of the microwave microplasma source.

3.2 Microwave Theory and Discharge Requirements

This section covers the transmission line and resonant cavity theory necessary for designing the plasma source. Discharge theory from Chapter 2 is used to derive the minimum performance requirements.

3.2.1 Breakdown Electric Field

The DC breakdown electric field was found using Paschen's law, a gap of $d = 100 \mu\text{m}$, and an air dielectric. Gas constants A and B , as well as γ , are used from two independent journal articles [55,56]. The A and B values are quite close, but the γ values have more variation. Since the breakdown electric field is related to the natural log of the natural log of γ , these differences are not of much concern. Table 3.1 summarizes the constants and calculated breakdown electric field for the gap described above.

We find a required electric field of just under $9 \text{ MV}\cdot\text{m}^{-1}$, noticeably higher than the approximately $3 \text{ MV}\cdot\text{m}^{-1}$ for breakdown at 1 atm of pressure over macroscale distances (e.g., 1 meter). Since we are using a $100\text{-}\mu\text{m}$ gap, this results in a required voltage of $\approx 900 \text{ V}$. As the gap distance is decreased, the required breakdown field increases as expected by Paschen's law. Using Equation 2.10 and an electric field of $9 \text{ MV}\cdot\text{m}^{-1}$, we find a critical frequency of 1.58 GHz and are, therefore, in the diffusion-controlled regime. The breakdown electric field in

Table 3.1: Breakdown Electric Field Parameters

Symbol	Description	Units	Source 1 [55]	Source 2 [56]
P	Pressure	Torr	760	760
d	Gap Distance	m	100×10^{-6}	100×10^{-6}
γ	SEY	unitless	0.005	0.02
A	Gas Constant	$\text{Torr}^{-1}\text{m}^{-1}$	1600	1200
B	Gas Constant	$\text{V}\cdot\text{Torr}^{-1}\text{m}^{-1}$	36000	36500
E_{bd}	Breakdown Electric Field	$\text{V}\cdot\text{m}^{-1}$	8.73×10^6	8.82×10^6

the diffusion-controlled regime is approximately one third that of the DC electric field, or $\approx 3 \text{ MV}\cdot\text{m}^{-1}$.

3.2.2 Transmission Line Model

This section covers the transmission line model, seen in Figure 3.2. A microwave power supply provides power to the plasma source through a SubMiniature version A (SMA) coaxial cable. An SMA “candlestick” is grounded to one parallel plate of the plasma source. The center conductor of the candlestick is then passed through the first plate and shorted to the opposing parallel plate of the plasma source. The center conductor then acts as a radiating probe that couples into the TEM mode of the parallel plate. One end of the parallel-plate transmission line is a short that defines the length of the resonant cavity and provides a path for heat conduction. At the opposing end is an open-circuit section, where two razor blades are mounted to create the $100\text{-}\mu\text{m}$ gap. The electric field distribution within the source will be noticeably different than a standard parallel-plate transmission line due to the conducting walls created by the razor blades, as will be seen later.

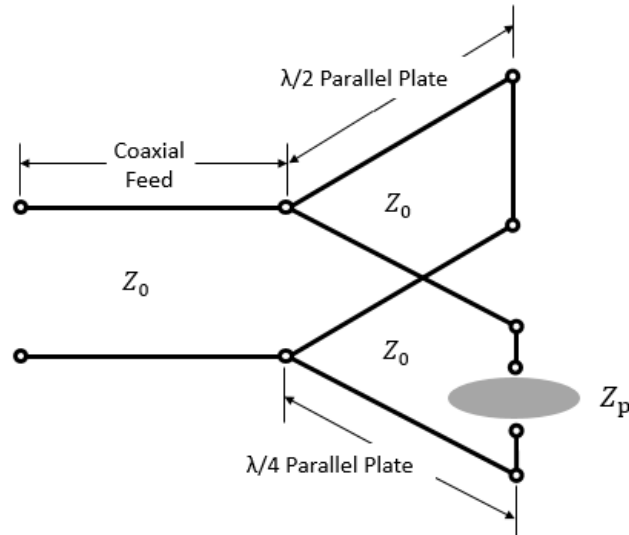


Figure 3.2: Transmission line model for the plasma source.

The physics behind the parallel-plate transmission line has been documented in several electromagnetics texts, for example [57]. Rectangular parallel plates, with a cross section like that of Figure 3.3, support propagation in the TEM mode and exhibit a characteristic impedance given by

$$Z = \sqrt{\frac{\mu}{\epsilon}} \frac{h}{w}, \quad (3.1)$$

where h is the distance between the plates, w is the width of the plates, ϵ is the absolute permittivity of the dielectric between the plates, and μ is the absolute permeability of the dielectric. This impedance equation is for the TM_n mode where $n = 0$, which yields the same field patterns as TEM propagation.

Previous work by H. Wheeler [58] in the 1960s gives a more exact solution to the parallel-plate problem and finds a width-to-height ratio of $w/h \approx 6.33$ for a characteristic impedance of $Z = 50 \Omega$. Using the ratio $w/h = 6.33$, and making the width of the plates equal to the width of the razor blades, we find a characteristic impedance of $Z = 59.6 \Omega$ using Equation 3.1. This impedance is in stark contract to that found by Wheeler, whose analytical approach includes the edge effects of the device. As a starting point for the design, we have used the value from the electromagnetics texts.

A critical assumption in both methods is that the plates are perfect electrical conductors. The intended material, copper, is sufficiently conductive that this assumption will not significantly affect design.

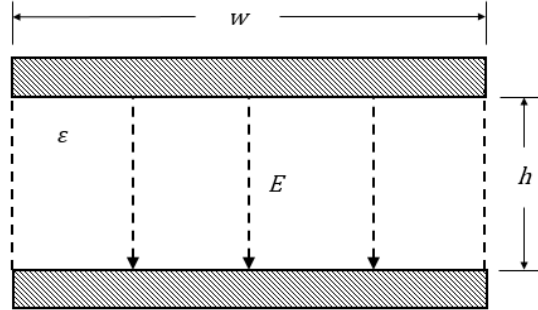


Figure 3.3: Dimensions and electric field distribution for a TEM mode parallel plate transmission line.

The distance from the feed to the gap will be set at one quarter wavelength at 2.45 GHz. The feed-to-short distance is then set to one-half wavelength, creating a three-quarter wavelength cavity that can sustain a standing wave. This creates a half-wavelength cavity for matching the open circuit during operation and leads to the highest electric field possible.

3.3 Electric Field Distribution of the Plasma Source

In this work, simulation was more time and cost effective than creating multiple prototypes. An electromagnetic model of the plasma source was created to estimate the electric field within

the gap. The model was created in COMSOL Multiphysics, a multi-physics software available through Penn State’s high performance computing group.

The first step was creating the physical model of the plasma source. Figure 3.4 shows the plasma source as modeled in COMSOL Multiphysics. The plasma source domains and boundaries were designated as copper. The coaxial feed was modeled as Polytetrafluoroethylene (PTFE) to match the dielectric found in the commercial SMA connectors that were used. Surrounding the source are air blocks that extend the model such that model boundaries will not effect the electric field patterns. The cavity dimensions are $61.2 \times 38.1 \times 5.05$ mm, which provides one quarter-wavelength distance between the radiating probe and the short and gap. The width was set by the razor blade’s dimensions and the height was determined using Equation 3.1 with $Z = 50 \Omega$. The overall source dimensions, including the razor blades, are $67.8 \times 38.1 \times 38.2$ mm.

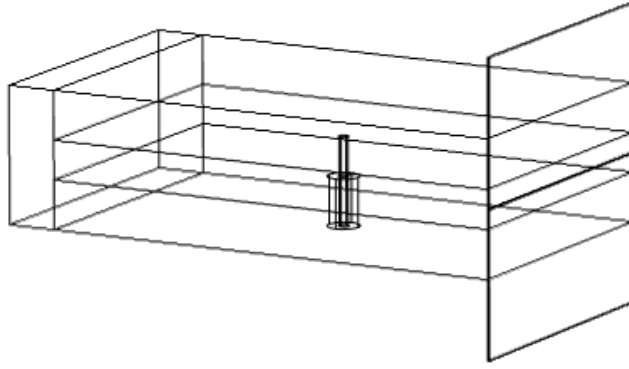


Figure 3.4: Wire frame model of the microwave microplasma source. Only the center conductor and dielectric of the SMA connector were modeled.

The source is excited using a coaxial port assigned to the PTFE boundary at the bottom of the source. At 1 W applied power, we found a gap electric field of approximately 100 kV/m. Figure 3.5 shows the front of the plasma source; the electric field within the gap appears as a black line in this figure due to the large aspect ratio between the length and thickness of the gap. Other views of the 1-W-excited source are found in Figures 3.6 and 3.7. The side view confirms TEM propagation through the coaxial portion and also reveals that the maximum electric field occurs at the gap electric.

Figures 3.8 and 3.9 present cartoons of the electric and magnetic fields created from simulation results. The electric field within the cavity resembles the TEM mode; however, there is a different field pattern near the electrodes. The gap appears to act like an electrically-small slit that is excited by a TEM plane wave, resulting in a diffraction pattern out of the front of the device. The magnetic field streamline reveals two local maxima at the gap. The magnetic fields at the gap may result in preferred areas for the plasma because charged particles favor movement along magnetic field lines, rather than across them.

The gap electric field increased to approximately 500 kV/m at 20-W applied power, indicating that the electric field is related to the square root of the applied power. The simulated field is an order of magnitude lower than the required breakdown electric field. This was not yet a

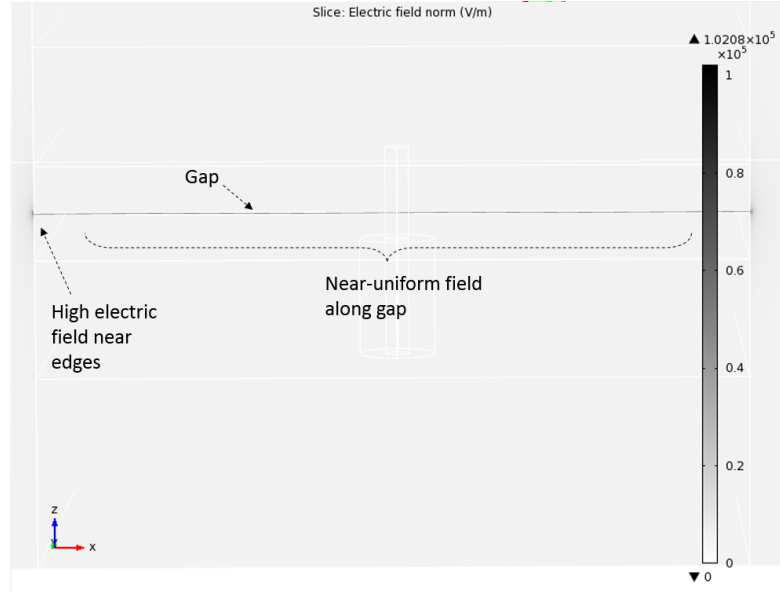


Figure 3.5: Front view of the plasma source electric field simulation at 1 W.

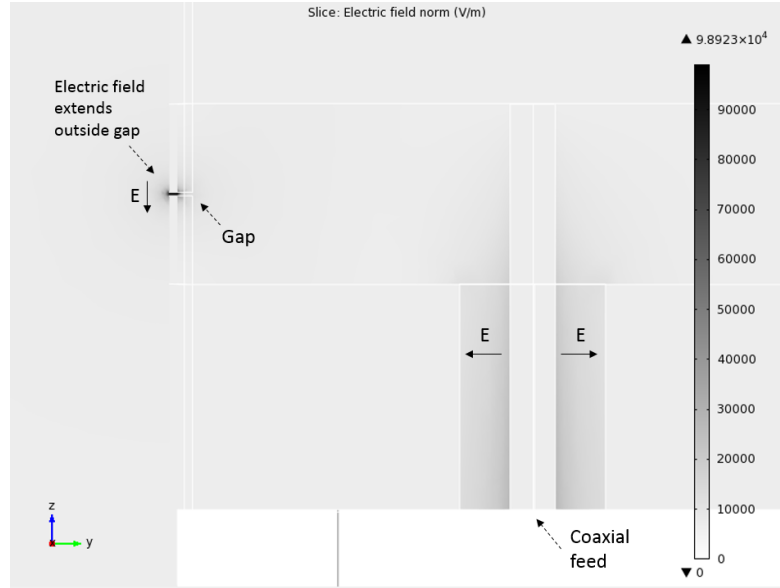


Figure 3.6: Side view of the plasma source electric field simulation at 1 W.

cause for concern, however, because the simulation model cannot be tuned as accurately as one would do with a tunable short without conducting a large parametric sweep. Optimizing the design further is possible using parametric sweeps available within COMSOL Multiphysics, but the non-idealities of a machined plasma source mean that these values will likely be incorrect. Thus, we have left the fine-tuning of the device as part of its construction.

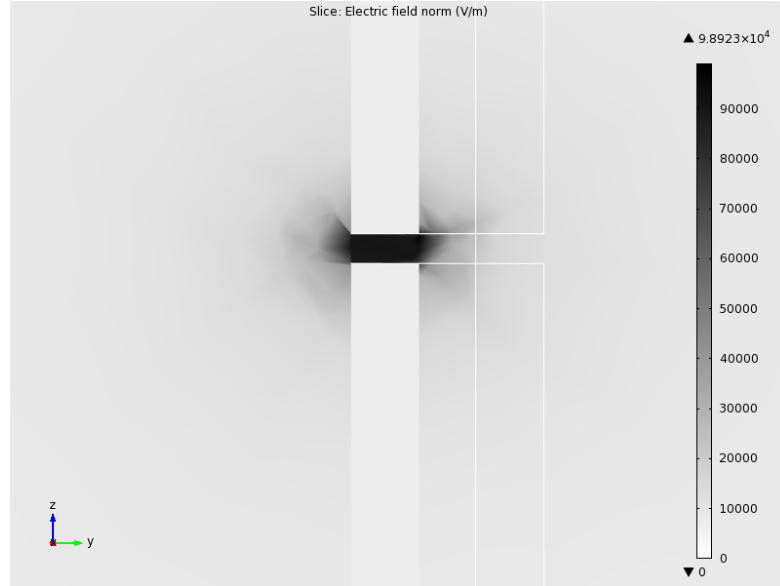


Figure 3.7: Side view of the microgap electric field simulation at 1 W. The high electric fields extend outward, but are strongest within the gap.

3.4 Physical Model and Tuning

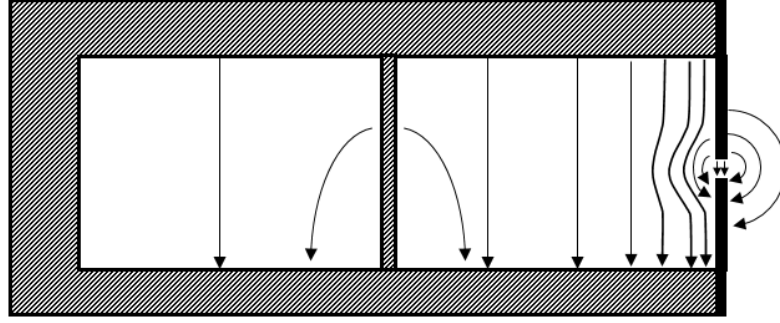
There were two main methods of creating the plasma source: a solid block of copper could be milled or several plates of copper can be joined together. The copper plate method was chosen to reduce waste and simplify machining. After simulation, a CAD model of the plasma source was drafted in SolidWorks. This model included the tap and clearance holes for constructing the device, as well as mounting the SMA connector and electrodes. Figure 3.10 shows a shaded model of the plasma source without screws, as well as an unshaded model with hidden lines visible.

A tunable short is included so that the device could be tuned to resonate at 2.45 GHz. A threaded rod was screwed in through the back of the plasma source and pushes/pulls a copper tuning block when turned. This method is not precise, but sufficient to move the copper tuning block into position when tuning with a vector network analyzer.

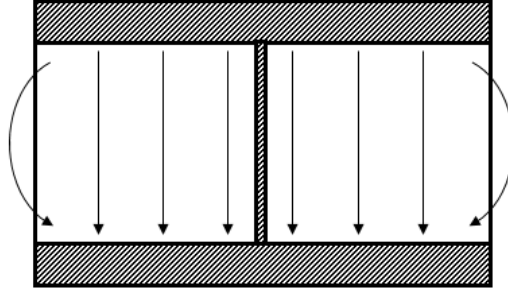
After design, the source was machined and assembled. The assembled device and a closer picture of the tuning section are shown in Figure 3.11. The tuning section was held together using string and copper tape for the first assembly, so it could be easily disassembled. A more rigid version uses punched copper sheet metal that holds the tuning screw against the tuning block.

3.4.1 Razor Blade Electrodes

Razor blades were chosen as a low-cost, easily-replaceable electrode. Two razor blades were screwed onto the device and were separated by a precision metal shim to create the gap. The stain-



(a) Side view: the electric field couples from the center probe into the parallel plate and increases towards the gap. A diffraction pattern is seen leaving gap.



(b) Front view (electrodes transparent): a TEM mode electric field distribution.

Figure 3.8: Electric field streamline cartoons for the front and side views of the plasma source. The cartoons were drawn from simulation results.

less steel razor blades are sufficiently electrically conductive ($\sim 10^6 \text{ S}\cdot\text{m}^{-1}$ [59]), which minimizes power loss. The razor blades are also sufficiently thermally conductive ($\sim 20 \text{ W}\cdot\text{m}^{-1}\cdot\text{K}^{-1}$ [59]) such that the razor blades will not begin to glow, instead, the heat is distributed throughout the copper plates. Sheet copper was also investigated, but cutting the metal left imperfect edges that would result in varying gap sizes and, thus, an uneven plasma.

3.4.2 PCB Electrodes

A second electrode design was created with the intent of having electrodes with consistent gap size, instead of having to space the electrodes by hand. The design, shown in Figure 3.12, consists of a copper-clad dielectric with the gap micromachined out of the material. The copper is milled away from the edges to leave only a dielectric structure and two holes are drilled for mounting onto the plasma source.

This design was not achievable using printed circuit board or thin film manufacturing due to insufficient milling resolution. Instead, laser or other precision micromachining is required. One caveat of laser micromachining is that the aspect ratio (thickness of material to the diameter of laser being used) must typically be under 10. For a $100\text{-}\mu\text{m}$ gap size, this means the board must be

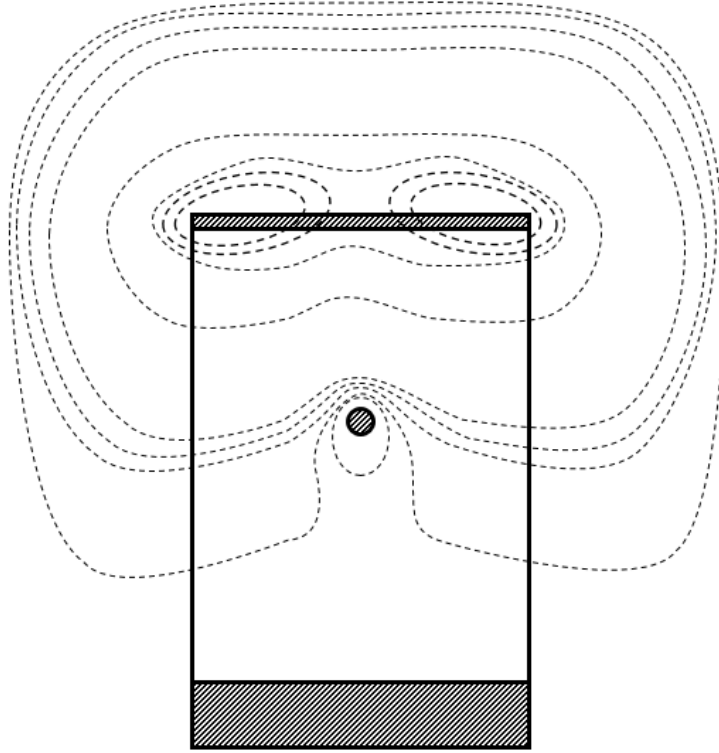
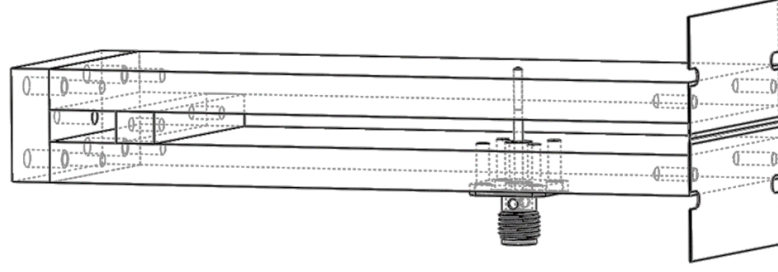


Figure 3.9: Magnetic field streamline cartoon for the top view of the plasma source. Two local maxima are found near the edges of the electrodes. The cartoon was drawn from simulation results.

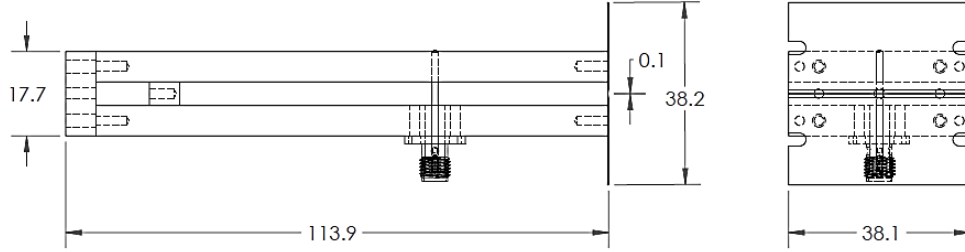
under 1 mm thick. Using a small flex or rigid-flex circuit board, it is possible to create a board less than 300- μm thick with a 1-oz copper pour (approximately 35 μm of the total thickness). While feasible, manufacturing these electrodes was prohibitively expensive for prototyping. However, production runs would amortize the initial setup costs over many units.

3.4.3 Reflection Coefficient

The reflection coefficient, S_{11} , was measured using a vector network analyzer. It was found during tuning that the SMA center conductor was not making adequate contact with the copper plate. After filling the hole with solder, the device performed as expected. Once tuned, the plasma source had a reflection coefficient of -24 dB, which means there would be approximately 0.4% reflected power before ignition. Figure 3.13 shows the source's S_{11} over the 2–3-GHz range. We further determined the device's performance as a resonator using the quality factor, or Q factor. The Q factor is related to the ratio of the energy stored per cycle and the power loss in the device; therefore, a higher Q factor indicates a more efficient resonator. Defining the Q factor as the center frequency divided by the 3-dB bandwidth of the reflection coefficient, we have the



(a) Unshaded with hidden lines. The holes are sized for UNC 3-48 taps.



(b) Major dimensions of the machined plasma source, in millimeters.

Figure 3.10: 3D and drawing views of the plasma source with major dimensions.

equation

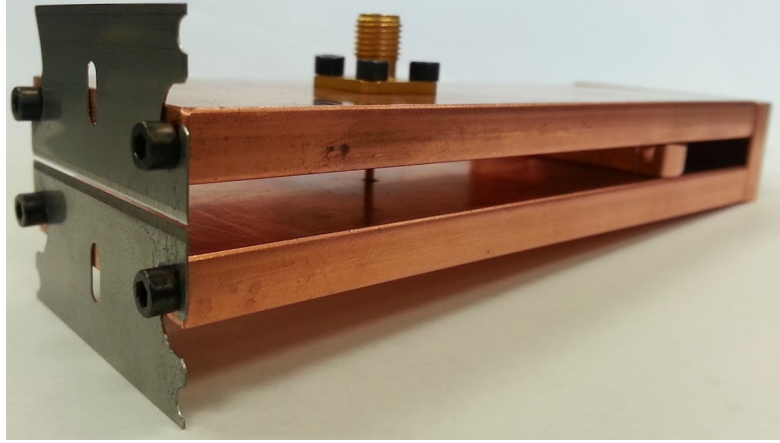
$$Q = \frac{f_0}{f_{\text{upper}} - f_{\text{lower}}}, \quad (3.2)$$

where f_0 is the center frequency and f_{upper} and f_{lower} are the frequencies above and below the center frequency that are 3 dB down (half power). Using this equation, the experimental values result in a Q factor of just under 82.

3.4.4 Ignition and Maintenance Power Testing

The ignition and maintenance powers of the plasma source, or equivalently the breakdown and minimum operating powers, were to be found through experimentation. However, the source did not self-ignite in any configuration without the use of a hand-held, high-voltage Tesla coil. The coil provides a high-voltage arc to breakdown the gas in the microgap in order to create the plasma, which is then sustained using microwave power. A diagram and picture of the test setup are shown in Figure 3.14. An Ophos 2.45-GHz microwave generator fed the device through coaxial cable and was specified to provide a maximum power of approximately 100 W. The actual power provided varied between 95–120 W. The applied and reflected power was measured using a Narda Model 3022 bidirectional coupler with 20-dB coupling that split power to two HP 8482A power sensors and HP power meters. The source was tested on a tabletop without an enclosure. After breakdown, the power was reduced until the plasma was extinguished, which marked the minimum maintenance power.

Spectral measurements were acquired using an Ocean Optics HR2000 spectrometer fed by an



(a) Assembled plasma source. Razor blades and a commercial SMA connector are used to lower cost and complexity.



(b) Close up of tuning section. A threaded rod pushes and pulls the tuning block, allowing us to change the cavity length.

Figure 3.11: Photographs of the assembled microplasma source.

optical fiber. The fiber end was placed 3 cm away from the plasma, normal to the front of the device. Spectral results and analysis are discussed in Chapter 4.

For the 100- μm gap, the source did not self ignite. The source partially ignited at 50 W using a hand-held Tesla coil and maintained plasma down to 30 W. However, the plasma was not uniform across the entire gap and the plasma length continued to decrease until it extinguished. The plasma spanned just over 7 mm at an applied power of 96 W. The razor blades sputtered near the edge, removing almost a millimeter of material, as is clearly visible in Figure 3.15, in addition to discoloration due to excessive heating. The plasma ignited first near an imperfection on the razor blades, likely due to the sharp edges causing high local electric fields. Changing the gap distance to 50 μm and 200 μm did not improve the performance of this configuration. There are two factors that may have prevented self-ignition: (1) the device has a low Q factor, and (2) the gap length is several times longer than previous designs [10,11], which would lead to a lower energy density.

For a second run we replaced the razor blades with 1/16-in sheet copper and moved to a 125- μm gap. Imperfections on the electrodes, such as uneven surfaces and gap distance, resulted

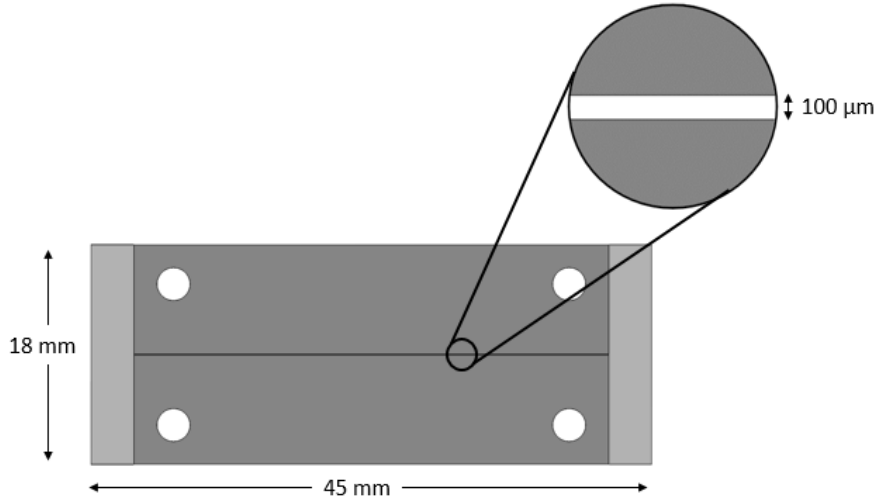


Figure 3.12: Flex PCB electrode design. A microgap is micromachined out of a copper-clad circuit board, providing better uniformity than hand-positioning electrodes.

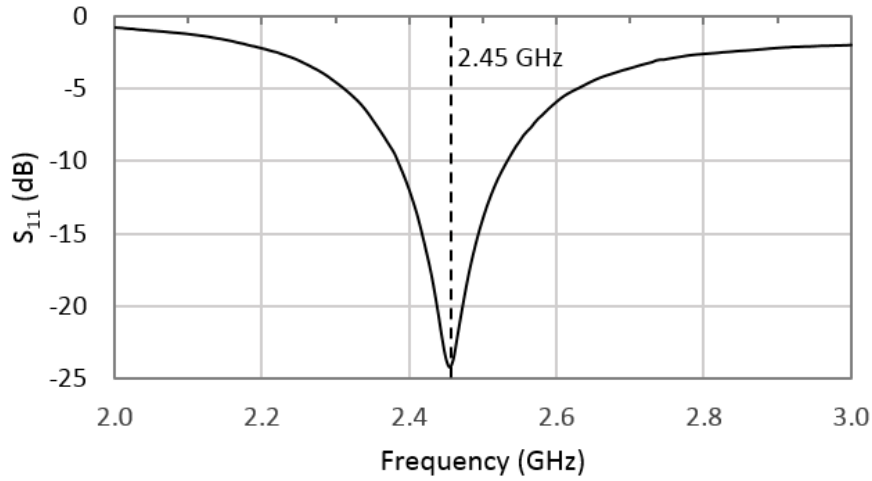


Figure 3.13: S_{11} of plasma source from 2–3 GHz using stainless steel razor blades.

in a lower reflection coefficient and a larger gap size than the desired $100\ \mu\text{m}$. After tuning, $S_{11} = -15\ \text{dB}$ and $Q = 36$ at resonance.

The plasma source with copper electrodes ignited at 70 W using a Tesla coil. The required power for ignition was increased as expected due to a worse Q factor and higher reflected power than with the razor blades. The copper electrodes produced a much larger plasma volume, with the plasma spanning 14 mm at 116-W forward power. Photographs of the plasma are shown in Figure 3.16. The photos provided are during the same experiment and show that the plasma volume moved during operation. The plasma ignited at a center portion of the gap but moved to an edge after two minutes of operation. A combination of heating, electrode erosion, and electric

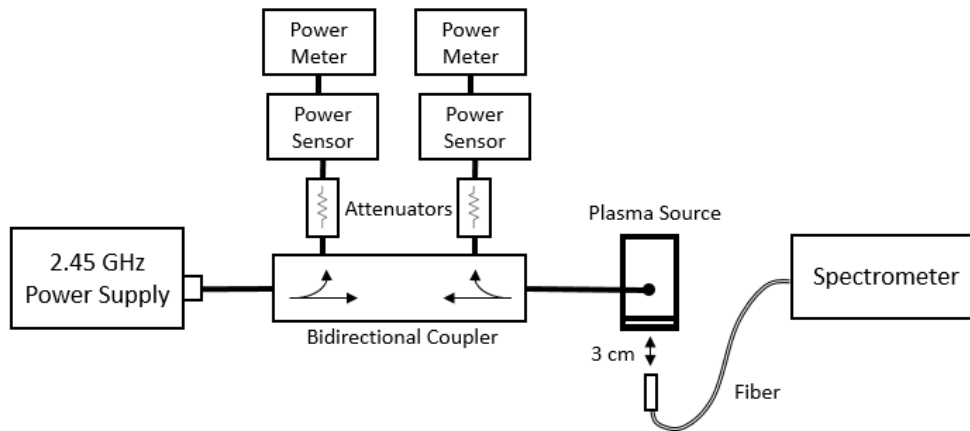
field pattern may have contributed to this shift.

3.5 Previous Designs

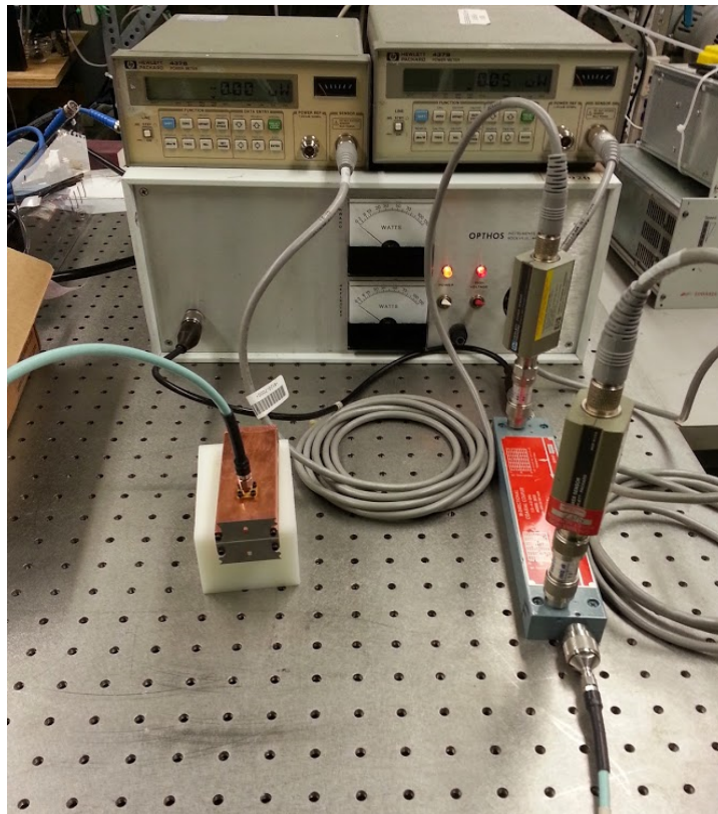
Prior to the final design, two different designs were constructed and tested. The first was a re-creation of the work done by Gregorio et al. (Gregorio 2009) and the second was a preliminary design of this model. For this section, all power values are the forward power.

Photos of the re-created source are in Figure 3.17. The source measured $89 \times 38 \times 17$ mm with a 15-mm gap length. The re-creation is a microstrip model instead of a parallel plate, meaning the ground plane is several times wider than the top plate. This source, therefore, would have a different height and width to achieve $50\text{-}\Omega$ impedance. The plasma, shown in Figure 3.18, was ignited using a Tesla coil. The plasma would sustain down to 15 W and experienced no sputtering until the power was increased to over 80 W. Plasma length increased with power and, while sustaining at 15 W, covered only 2 mm of the total electrode length. The plasma length was 9 mm at 70 W, but greater power could not be applied because the electrodes were positioned using copper tape that would begin to burn and peel off above 75 W.

The preliminary design for this thesis is shown in Figure 3.19 and its operation in Figure 3.20. The source measured $82.5 \times 38 \times 18$ mm with a 38-mm gap length. This source failed to ignite, but could sustain a plasma after using the Tesla coil to ignite. The source was tested using both copper and razor blade electrodes. The copper electrodes were made from sheet copper and resulted in an uneven plasma distribution due to imperfect construction, where the plasma favored locations where the gap was smaller. The plasma would sustain down to 30-W forward power where it spanned approximately 2 mm of the electrode length. At higher powers, discoloration occurred in the razor blades. A second source, detailed in the previous sections, was required because there was insufficient tuning range on the first device to achieve resonance.



(a) Schematic of test setup. A 2.45-GHz microwave generator feeds power to the plasma source through a coaxial cable. The forward and reflected powers are measured using a bidirectional coupler that directs power to two HP8482A power sensors.



(b) Implementation of the test setup without the optical fiber. Testing was done on an optical table.

Figure 3.14: Power and spectral measurements setup.

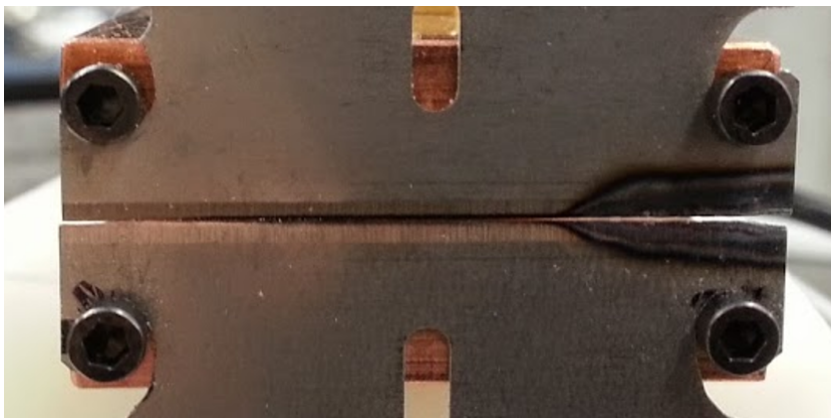
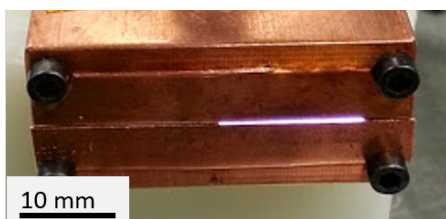
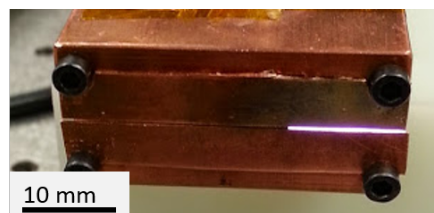


Figure 3.15: Plasma source after sputtering has removed material.



(a) Immediately after ignition

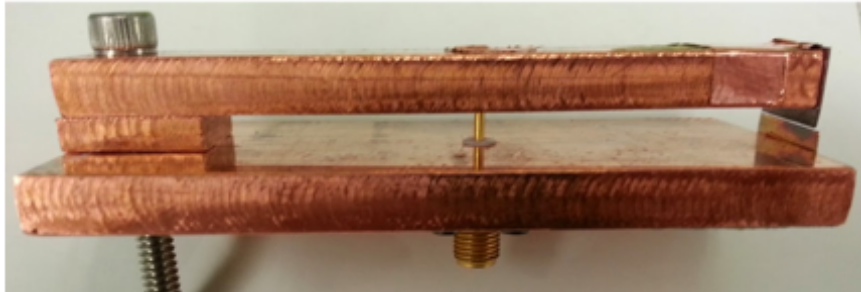


(b) After 2 minutes of operation

Figure 3.16: Plasma volume using copper electrodes and 116-W applied power.

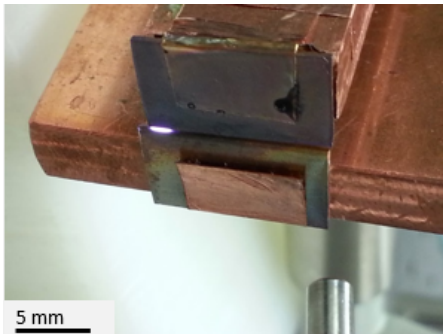


(a) Front view

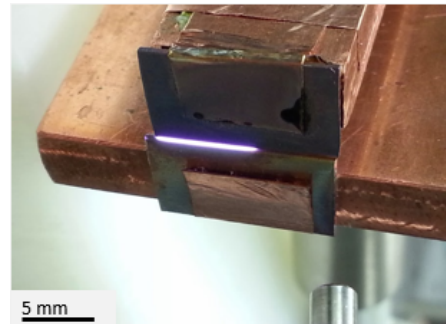


(b) Side view

Figure 3.17: The microstrip plasma source using electrodes made from 1/32 in copper sheet.



(a) 15 W



(b) 70 W

Figure 3.18: Microplasma from the re-created source at varying applied power.

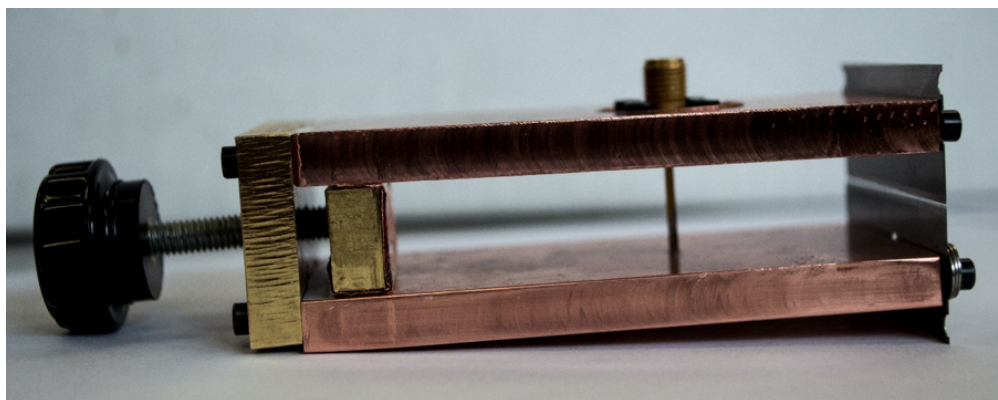
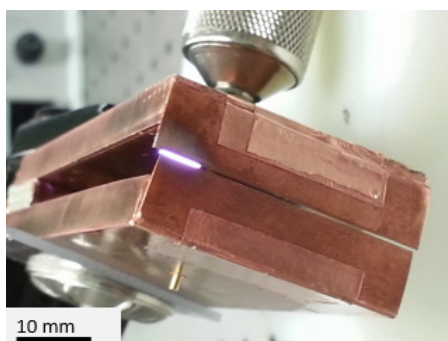
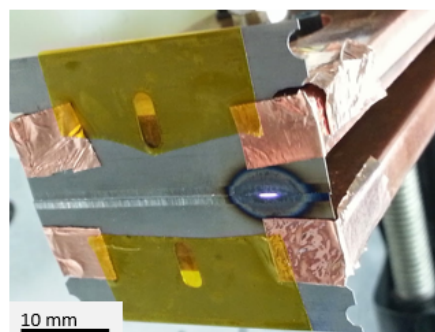


Figure 3.19: Preliminary source design with tunable short and razor blade electrodes.



(a) Copper



(b) Stainless steel

Figure 3.20: Microplasma from the preliminary design using copper electrodes and stainless steel razor blades.

Chapter 4

Results

This chapter covers a brief analysis of the emission spectrum, as well as measurements to determine the generated heat and ozone.

4.1 Emission Spectrum: Observations and Analysis

The plasma emission spectrum was recorded using an OceanOptics HR2000 spectrometer at 0.5-nm full-width-at-half-maximum (3-dB bandwidth) resolution. Emissions were collected using a fiber placed 3 cm away from the plasma volume. Figure 4.1 shows the spectrum from 200–1000 nm after background subtraction, with labels for the dominant particle transitions. It is clear that the N_2 SPS spanning 300–500 nm dominates the gas, but there is significant overlap with the neighboring N_2^+ FNS. The nitrogen FPS is also visible in the 500–900 nm range.

In addition to the nitrogen systems, there are strong lines for the NO_γ system below 300 nm and the atomic oxygen triplet at 777 nm. It is likely there is large overlap between the NO γ - and β -systems and the N_2 SPS due to the suggested presence of NO and the low wavelength resolution. A closer analysis of the spectrum shows small peaks just above 300 nm that suggests the presence of the $OH(A-X)$ system.

4.2 Gas Production and Thermal Properties

We first characterized the source by looking at the heat generated during operation. The temperature of the copper plate with the SMA attachment was measured *in situ* with an Analog Devices TMP36G band-gap temperature sensor placed 2 cm away from the gap. The temperature sensor output was sampled at 20 Hz using a National Instruments MyDAQ and a LabVIEW VI that may be found in Appendix C. The temperature of the copper was recorded over a 10-minute interval, but much of the data is unusable due to coupled noise from the applied microwave power. The copper quickly became too hot to handle safely and the temperature increased to 119 °C after 10 minutes of operation. Therefore, future designs looking to implement these plasmas over long periods of time should investigate heat management such as air cooling and heat sinks.

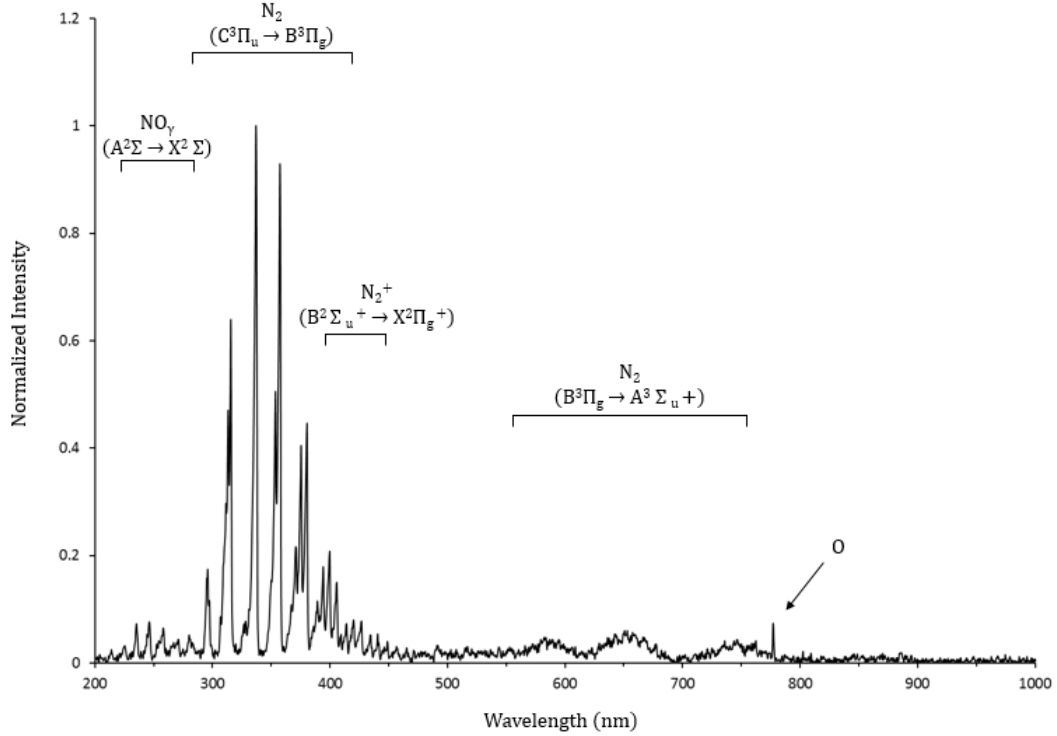
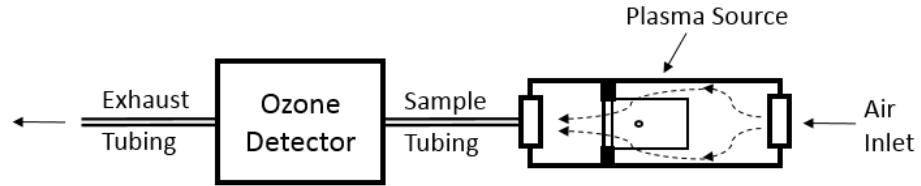


Figure 4.1: Normalized microplasma spectrum from 200–1000 nm.

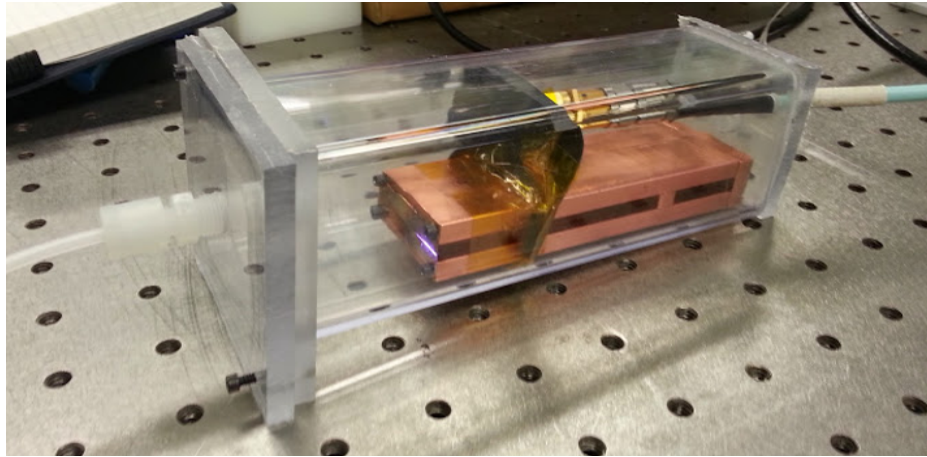
In addition, thermal measurements should be taken with more noise-immune devices, such as thermal cameras and fluoroscopic sensors.

The plasma source’s ozone production was measured using a Teledyne-API Model 450M UV absorption-based ozone detector. For this test, the source was placed in a clear polycarbonate chamber connected to the ozone detector by a 1.2-m-long, 1/8-in-diameter PTFE tube. A flow rate of $1.5 \text{ l}\cdot\text{min}^{-1}$ is set by the detector’s internal vacuum pump to provide adequate flow past the source. The flow rate is measured using the indicator on the detector. The chamber was designed such that the air is forced past the gap before continuing to the ozone detector so that we measure the air passing the plasma rather than the ambient air. Figure 4.2 is a schematic of the ozone test setup and a photograph of the polycarbonate chamber.

The measured ozone generation at 96-W applied power was approximately 0.002 %wt with this testing configuration. The concentration was $21 \text{ ppm} \pm 0.1 \text{ ppm}$ at the detector. This result is considerably lower than that of commercial ozone generators at the same power. Note that the error term is derived from the detector’s performance and, therefore, not indicative of the total error in the system. Air leaks around the source and ozone recombination within the chamber and tubing likely contributed to a lower concentration at the detector. The measured concentration is comparable to a microgap powered by 1kV/25-Hz AC, reported by Kazuo Shimizu [60], that operated at less than 10 W. While our microwave solution does not require high-voltages during operation, we require a higher applied power for similar ozone production. To date, the ozone



(a) Diagram of ozone test setup



(b) Ozone test chamber

Figure 4.2: Ozone test configuration and chamber during operation.

production of the PCB split-ring and linear resonators has not been determined. Therefore, we may not make any comparisons to other microwave microgap designs.

Chapter 5 |

Improving Plasma Diagnostics Capabilities

Laser-based diagnostics are necessary to better characterize microplasmas. This chapter covers two well-documented laser-plasma mechanisms: fluorescence and scattering. A preliminary system design for use with microplasmas is presented for both mechanisms.

5.1 Laser Diagnostics and Scattering Theory

Research into microplasmas requires minimally invasive diagnostics. Langmuir probes and other *in situ* measurements are capable of significantly changing the system under test and, thus, influence measurements. These changes may be caused, for example, by physical obstruction or the application of electric fields. In addition, the probes may be too large to access the plasma, such as when measuring millimeter-scale dielectric barrier discharges and microgap plasmas. Laser diagnostics offer an alternative solution with improved spatial resolution and measurement accuracy.

5.1.1 Laser Induced Fluorescence

Laser induced fluorescence (LIF) is a spectroscopic technique to determine the number density of a neutral species in a gas. Just as particles emit light at specific wavelengths when bound electrons relax, the bound electrons can also be excited to higher energy levels by applying a laser at specific wavelengths. After excitation, we may then detect the light emitted when the excited particle relaxes. This emission is known as fluorescence. Figure 5.1 shows an example single-photon fluorescence event, where the particle is (1) excited by a laser photon, (2) undergoes vibrational relaxation to an intermediate state, and (3) returns to the ground state by emitting a photon.

This section covers disperse-spectra LIF techniques, which uses a fixed laser wavelength; however, there is also an excitation scan technique that requires scanning the laser and detecting at a fixed wavelength or range of wavelengths. A simple disperse-spectra LIF system involves exciting

Table 5.1: LIF Parameters for Common Reactive Plasma Species

Particle	Technique	Excitation Wavelength	Detection Wavelength
O	TP-LIF	226 nm	845 nm
N	TP-LIF	211 nm	869 nm
OH	SP-LIF	283 nm	308 nm
NO	SP-LIF	226 nm	247 nm
NO ₂	SP-LIF	435 nm	780 nm

a particle using a laser and recording the emitted photons, which are typically a longer wavelength than the laser light due to the particle undergoing vibrational and rotational relaxation before emitting. The red-shift due to vibrational relaxation is referred to as a Stokes shift. The detected light intensity can be integrated over a range of wavelengths to yield a temporally-resolved intensity measurement. The lifetime of the signal is then related to the number of particles excited as well as the collision rate and other quenching effects.

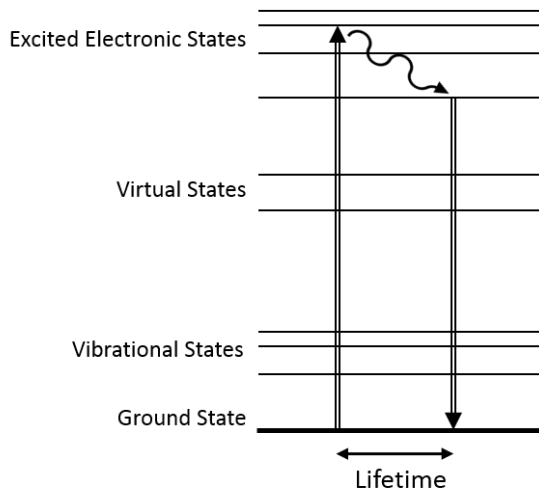


Figure 5.1: The fluorescence process.

There are several different techniques within LIF. In single-photon LIF (SP-LIF), the particle of interest is excited from the electronic ground state by absorbing a single photon. In contrast, two-photon LIF (TP-LIF), also called two-photon absorption LIF (TALIF), relies on the simultaneous absorption of two photons by a single particle. SP-LIF often requires photons in ultraviolet spectrum; however, we may use TP-LIF for the same excitation by doubling the laser wavelength and, therefore, reducing laser requirements. The TP-LIF technique is particularly beneficial for atomic oxygen and nitrogen. For example, atomic oxygen (O) may be excited at 225.7 nm in the short-wave ultraviolet (UV-C), instead of 112.8 nm in the vacuum ultraviolet. The SP-LIF signal is proportional to the laser intensity while the TP-LIF is proportional to the square of the laser intensity, although TP-LIF is less efficient. Table 5.1 provides a list of common plasma species and their absorption wavelengths for SP-LIF and TP-LIF.

A single-species LIF system requires a pulsed laser tuned to the excitation wavelength of the species of interest, optics and filters, and a detector. The detector does not need to resolve wavelengths, so a single photo-multiplier tube (PMT) can be used instead of a spectrometer or CCD. Figure 5.2 shows a schematic of a LIF system for measuring a single species.

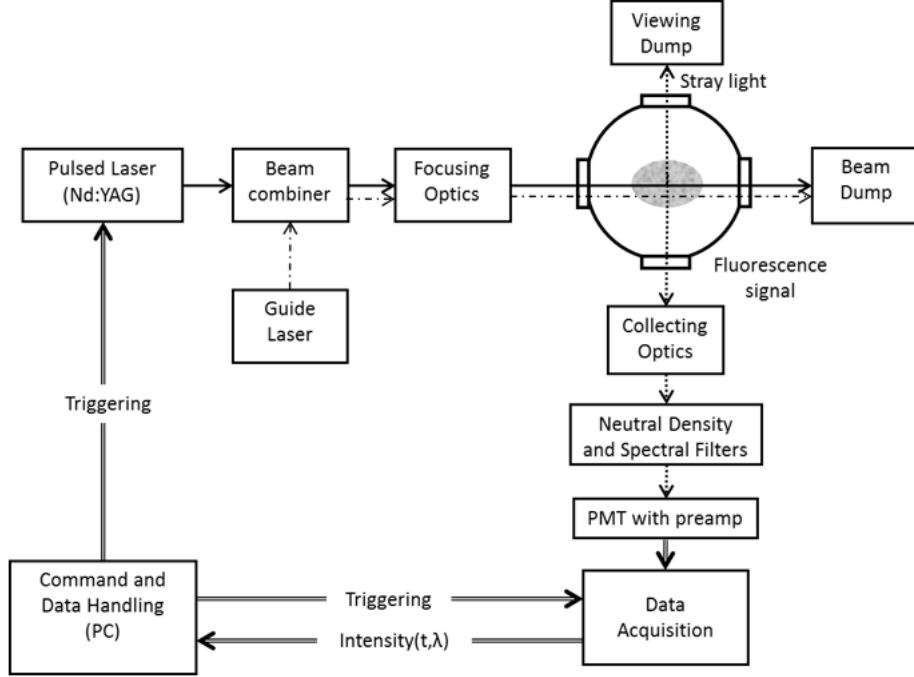


Figure 5.2: A LIF system for detecting a single species. A pulsed laser is used to excite a plasma within a chamber, causing LIF. The LIF signal is then observed through collection optics and a photomultiplier tube. The spectral filter removes stray light and, by changing the neutral density filter, the system may measure at different number densities and laser pulse energies.

5.1.2 Rayleigh, Raman, and Thomson Scattering

The application of a laser to plasma results in three primary scattering effects: Rayleigh scattering, the elastic scattering of photons from bound electrons; Raman scattering, an inelastic scattering caused by energy level transitions; and Thomson scattering, a special case of Compton scattering in which free electrons oscillate due to incident radiation and emit as dipoles. Example energy level transitions involved in scattering are shown in Figure 5.3. Each scattering phenomena yields unique plasma characteristics, but at varying spectral widths and signal strengths. Table 5.2 summarizes the scattering phenomena and what plasma characteristics can be derived. This research is interested in the Raman and Thomson scattered signals in order to find electron temperature and density as well as neutral densities. The production of specific neutral gases, such as ozone, can be determined using the Raman scattered signal.

In Thomson scattering, an incident wave accelerates free electrons that then radiate at the

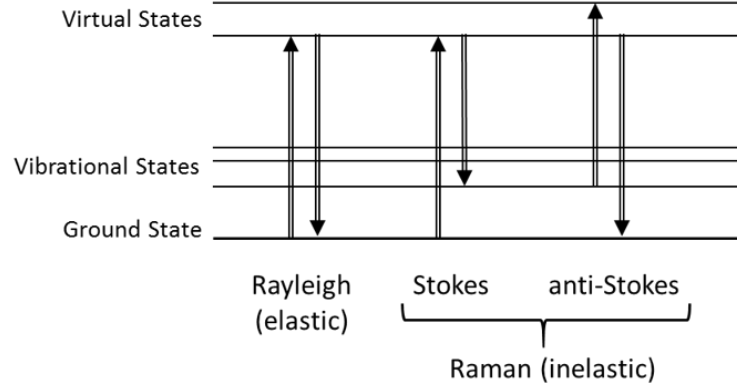


Figure 5.3: Rayleigh and Raman scattering processes.

Table 5.2: Types of Scattering and Derived Plasma Parameters

Scattering Type	Plasma Parameters
Rayleigh	Gas Temperature, T_g
Raman	Rotational Temperature, T_{rot}
	Molecular Densities of Neutral Particles, n_M
Thomson	Electron Temperature, T_e
	Electron Density, n_e

same frequency. If the electrons undergo thermal motion, then a Doppler shift will occur. The scattered signal is, therefore, dependent upon the thermal energy of the free electrons. A higher thermal energy, and thus velocity, will lead to a larger Doppler shift and wider signal. If the electrons have a Maxwellian velocity distribution, then the scattered signal will be Gaussian about the incident laser frequency. From the scattered signal, we can then relate the full width at half maximum to the electron temperature and the total scattered signal intensity to the electron number density. The electron number density requires calibration using a Raman scattered signal or using another laser at a different excitation wavelength.

There are two Thomson scattering regimes: coherent and incoherent. In order to obtain the full distribution of Doppler shifts, the incident laser must have a sufficiently small wavelength to be in the incoherent regime. If the wavelength is too large, then the phase difference between nearby electrons is negligible. The radiation will then add up coherently, which will provide information about the collective behavior of the plasma, but not electron temperature. This means that the excitation laser must have a wavelength, λ , much smaller than the plasma Debye length, λ_D .

Raman scattering requires analysis of a particle's energy level transitions. Unlike Rayleigh scattering, an elastic process, Raman scattering is inelastic because of changes in the rotational and vibrational state of the particle being excited. This phenomenon is known as Stokes and anti-Stokes scattering and is illustrated in Figure 5.3. The population of states follows a Boltzmann distribution based on the rotational temperature of the gas. Therefore, we can determine

the rotational temperature based on the observed transitions. While this method assumes a Boltzmann distribution and is, therefore, not accurate for a nonequilibrium plasma, it may still provide a reasonable estimate of the temperature.

5.2 Preliminary Design of a Laser Scattering System

This section will cover the design of a Thomson and Raman scattering system for characterizing microplasmas. We first determine the laser requirements using photon statistics and then discuss the experimental setup and supporting equipment.

5.2.1 Laser Selection

A low-cost and popular laser is the Nd:YAG (neodymium-doped yttrium aluminium garnet), operating at 1064 nm and frequency doubled to 532 nm.

Assuming an electron temperature of 10 eV and number density of 10^{20} m^{-3} , a microplasma has a Debye length of approximately $2.4 \text{ } \mu\text{m}$. The scattering parameter is then within the incoherent regime at $k\lambda_e = 28$ if using a 532-nm Nd:YAG laser.

The required laser pulse power depends upon the detector system and scattering cross section of the plasma. For this application, assuming 5-ns gating on an intensified charge coupled device (ICCD), we find a required energy of 1 mJ/pulse for 8-dB signal-to-noise ratio (SNR). The SNR was calculated using the expression from Hutchinson [61]:

$$\text{SNR} = \left[\frac{h_p c}{2C \sin\left(\frac{\theta}{2}\right) \sin(\theta)} \right]^{1/2} r_e^2 N_i \left[\frac{\Omega_s L_s}{d_l L_c \Delta t} \right]^{1/2} \frac{T_e^{1/4} Q_e^{1/2}}{Z_{\text{eff}}^{1/2}}, \quad (5.1)$$

where

h_p	Planck's constant;
c	speed of light;
C	bremsstrahlung factor;
θ	scattering angle;
r_e	classical electron radius;
N_i	number of incident laser photons;
Ω_s	collection optics solid angle;
L_s	length of the scattering volume;
d_l	laser beam diameter;
L_c	optics distance from the scattering volume;
Δt	pulse and gating duration;
T_e	electron temperature;
Q_e	product of the optical transmission and detector quantum efficiencies;
Z_{eff}	effective ion charge.

The ICCD gating time must be small in order to limit the stray light and plasma light (e.g., bremsstrahlung photons) entering the detector. Strong line radiation contributes to the plasma light and has been shown to decrease SNR by up to a factor of 500, or 27 dB [61]. A spreadsheet for determining SNR based on experimental parameters was used to find a minimum pulse energy and can be found in Appendix D. The pulse energy and duration are close to the those recently used by a Thomson scattering system for helium microplasma measurements [62].

5.2.2 Laboratory Setup and Electronics

A design for the scattering experiment is shown in Figure 5.4. There are two possible designs for the spectrometer. First, as shown in Figure 5.4, is the use of a ultra-narrow bandpass filter to block the Rayleigh-scattered and stray laser light. This allows us to use a simpler spectrometer, but requires a filter with a bandwidth much less than the Thomson-scattered signal that spans only a few nanometers. The second option is to use a triple grating spectrometer (TGS) that removes the laser light using a mask inside the spectrometer. There are performance benefits with using a TGS system due to improved stray light rejection, but a TGS is also more costly.

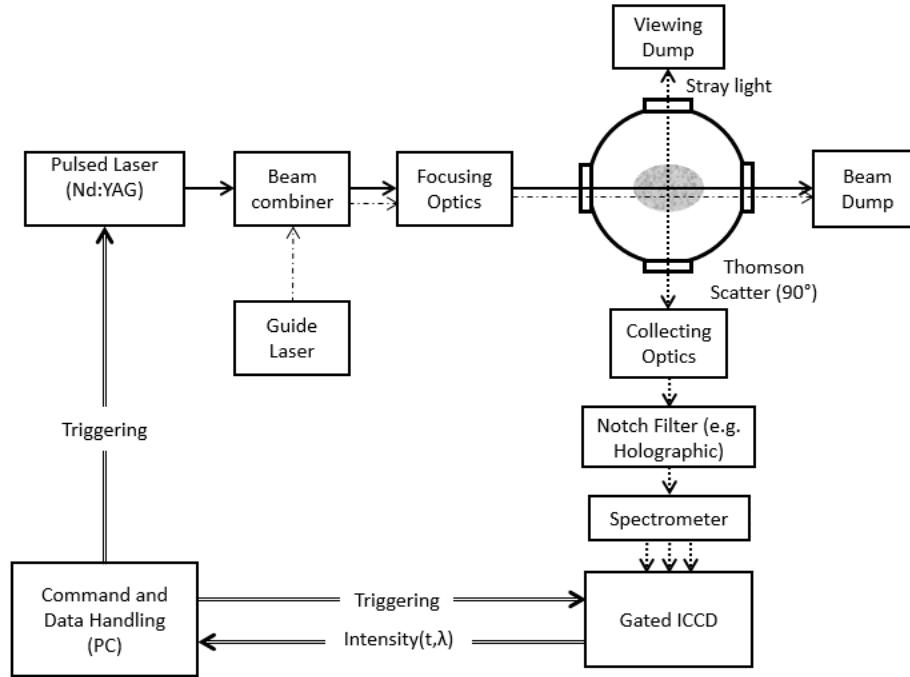


Figure 5.4: Schematic of a laser scattering system. A pulsed laser, in the visible range, is scattered by the plasma volume. Measurements are taken at a 90° scattering angle and the Rayleigh scattered signal is removed using a notch filter, leaving only the Thomson and Raman scattered signals. Unlike a LIF-system detector, the detector for scattering measurements must resolve the spectrum. Therefore, an ICCD is chosen over a photomultiplier tube.

The electron temperature measurements do not require calibration, whereas the density measurements must be calibrated by analyzing the Raman-scattered signal of a known gas. This

calibration can be done using a chamber filled with gas, such as air or pure nitrogen, at known temperature and pressure. After calibration, a test article may be placed within the chamber and aligned with the pulsed laser by making use of a low-power, visible guide laser. After passing through the plasma volume, any non-scattered laser energy is directed towards a beam dump.

A personal computer is sufficient to control the system, and a delay/pulse generator would provide the triggering to align the laser pulse and detector gating. Several measurements are taken and integrated to form a distribution for analysis. Integrating over multiple measurements is necessary due to the small number of scattered photons per laser pulse in microplasmas, but integration times may be lessened or removed by increasing the laser pulse energy or cross-sectional area of the laser-plasma interaction. The recorded spectrum is a superposition of the Thomson and Raman scattered signals that, if the electron thermal velocity distribution is known, may be separated and analyzed individually. Fitting techniques have been explored for non-Maxwellian electron thermal velocity distributions and are still under investigation [63–65].

Chapter 6 |

Conclusions and Future Work

This thesis has presented the design and testing of a microwave microplasma source for ozone generation. At 116-W applied power, the plasma spanned 14 mm of a 100- μm gap and produced 0.002 %wt ozone, with a copper temperature of up to 119 degC after operating for 10 minutes. The design's performance was inadequate for the intended application based on the unsafe operating temperature and low ozone production rates. In addition, source ignition required the use of a high-voltage arc from a Tesla coil, removing one major benefit of using microwave power over DC and low-frequency AC. Through spectral analysis, we have identified reactive species including OH, NO, and O, which may lead to applications outside of water treatment.

We have also described an effort to expand our research group's plasma diagnostic capabilities by developing laser-based systems. These systems, using laser-induced fluorescence and laser scattering, can be used for a variety of microplasmas and larger atmospheric-pressure plasma sources to determine plasma and neutral gas parameters, providing researchers with insight into the gas species and temperatures.

Before considering configurations such as a plasma line, the design has two primary issues that must be addressed:

1. The increase in source temperature beyond what is safe to handle, and
2. The need for a Tesla coil to ignite the plasma.

Potential solutions include better machining practices and smaller source dimensions, which should maximize the Q factor and limit the amount of microwave power radiated from the open sides of the parallel plate configuration.

The source must also be further characterized by finding the gas temperature through optical emission spectroscopy or other techniques. Gas flow configurations may also be explored in order to change the plasma properties. For example, new gas flow configurations could change the amount of time particles are within the plasma volume, which would lead to different gas temperatures. A final concern to address is verifying the %wt ozone measurement. A leaky seal around the source and the recombination of ozone before entering the detector may result in lower-than-expected concentrations.

Appendix A |

COMSOL Multiphysics Notes

This appendix is for users who wish to recreate the design or analyze similar devices in COMSOL Multiphysics. These notes are valid for all 4.x versions of COMSOL Multiphysics.

A.1 Materials

All device domains were assigned copper and had copper boundaries. The air dielectric and air blocks were assigned air domains and air boundaries. The outer walls of the simulation default to perfect electrical conductors, so care must be taken to ensure that you are not receiving reflected fields near the device. PTFE was manually entered as a material, while copper was taken from the COMSOL Multiphysics materials database.

A.2 Port Excitation

The coaxial port excitation was assigned to the boundary between the inner and outer coaxial conductors, which is an annular ring of Teflon. A 1D plot of S_{11} over frequency can be obtained by creating a 1D global plot through the Results section.

A.3 Meshing

The model was meshed in two parts. The razor blades and gap section were meshed first using a tetrahedral with minimum size of 10^{-5} meters. The rest of the model was then meshed with a minimum size of 10^{-4} to reduce computation time.

A.4 Parametric Sweeps

Range entries for parametric sweeps can occasionally result in errors when using a large number of points or optimizing over two or more parameters. It is recommended to sweep one parameter at a time with a manually entered range of numbers. That is, you would want to enter the range

as (0.0, 0.1, 0.2, 0.3, 0.4) rather than range (0, 0.1, 0.4). Ensure that Job Configurations has been cleared between sweeps.

A.5 Solving and Plotting

The solver was set to solve only at 2.45 GHz. Expect simulation to take several minutes or longer due to the fine mesh at the microgap. The plots in this thesis were obtained using slices of the normalized E field.

Appendix B |

Plasma Source Drawings

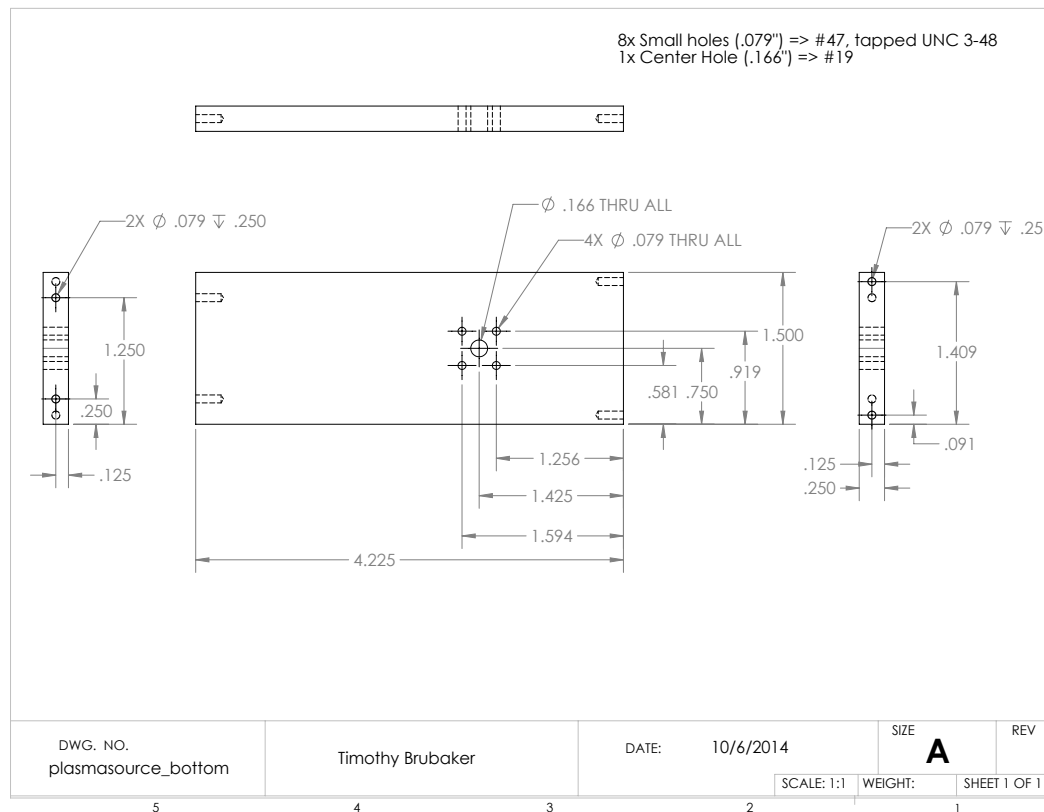


Figure B.1: Bottom plate of plasma source.

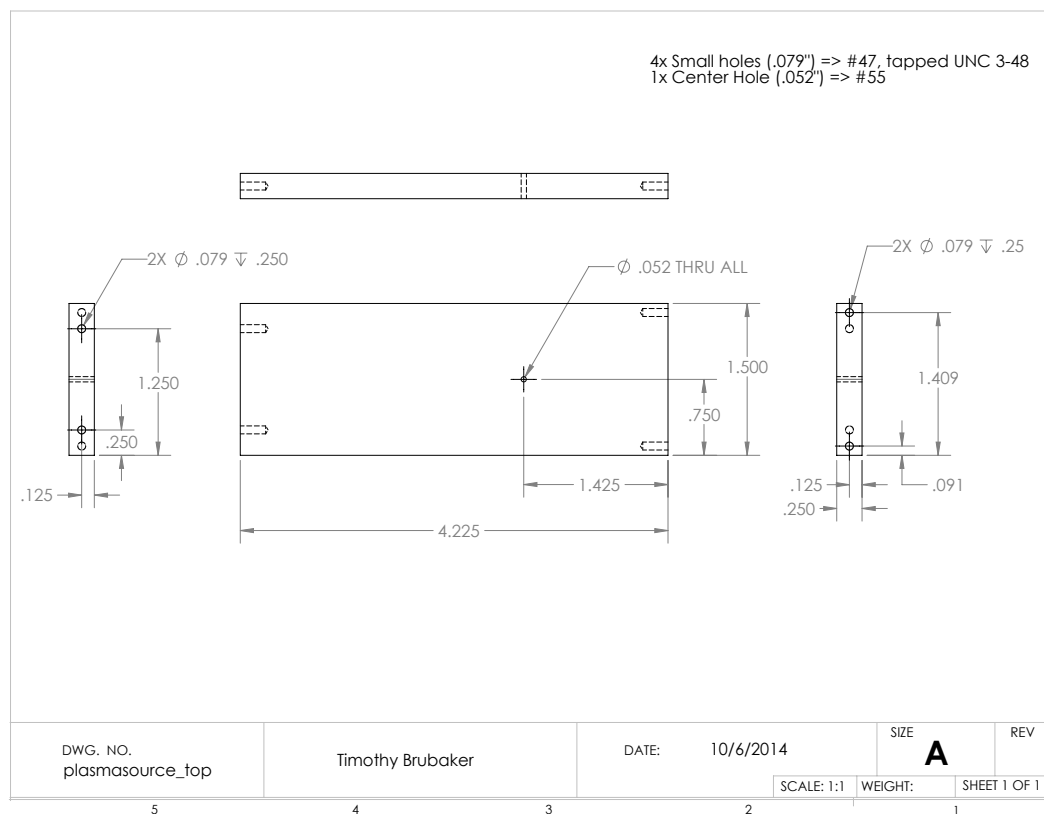


Figure B.2: Top plate of plasma source.

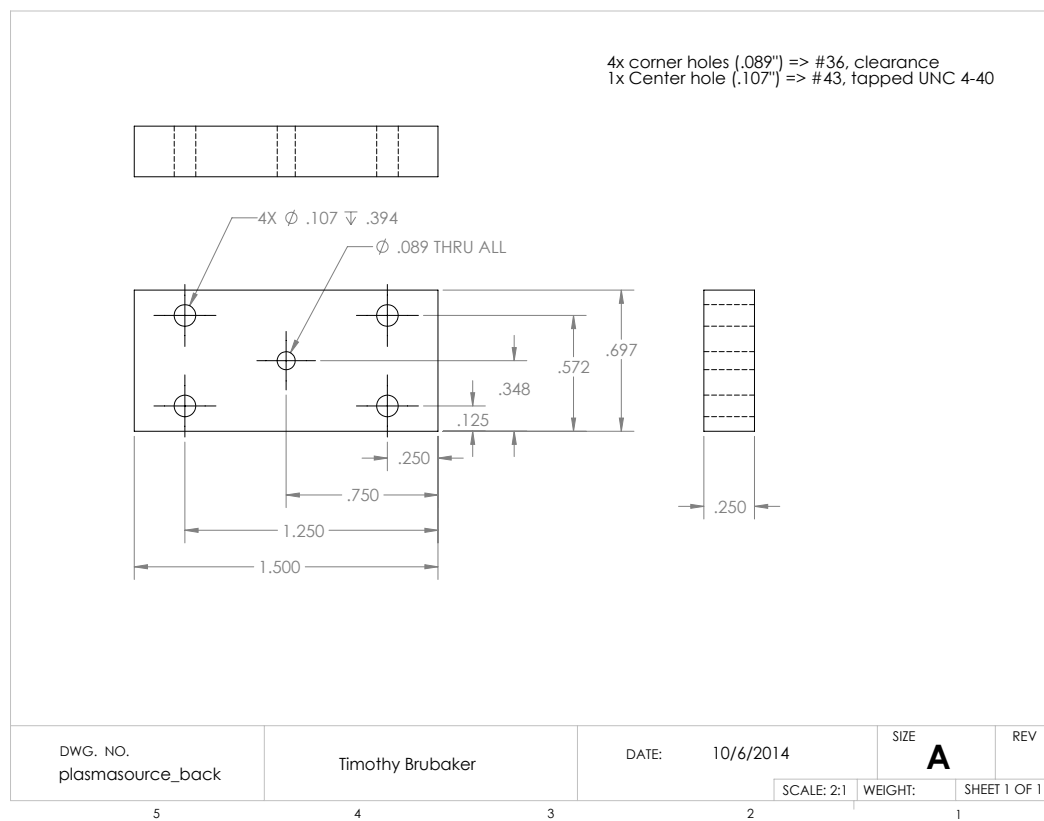


Figure B.3: Back plate of plasma source.

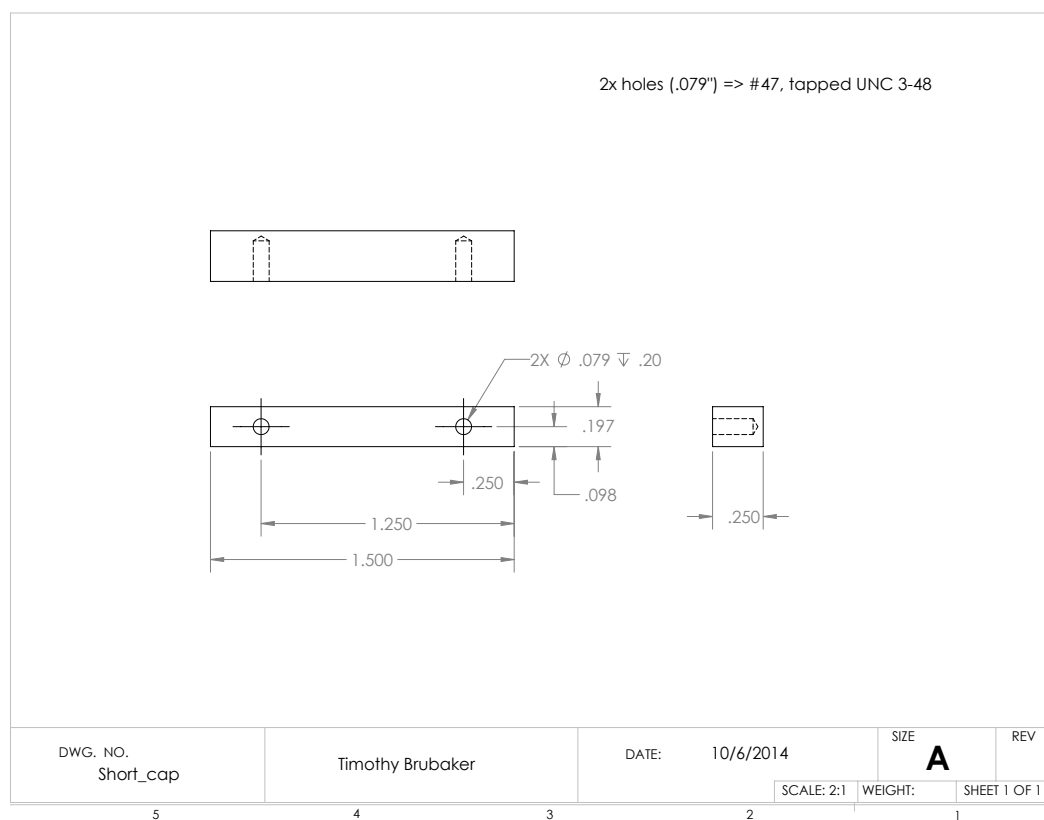


Figure B.4: Shorting block for tuning.

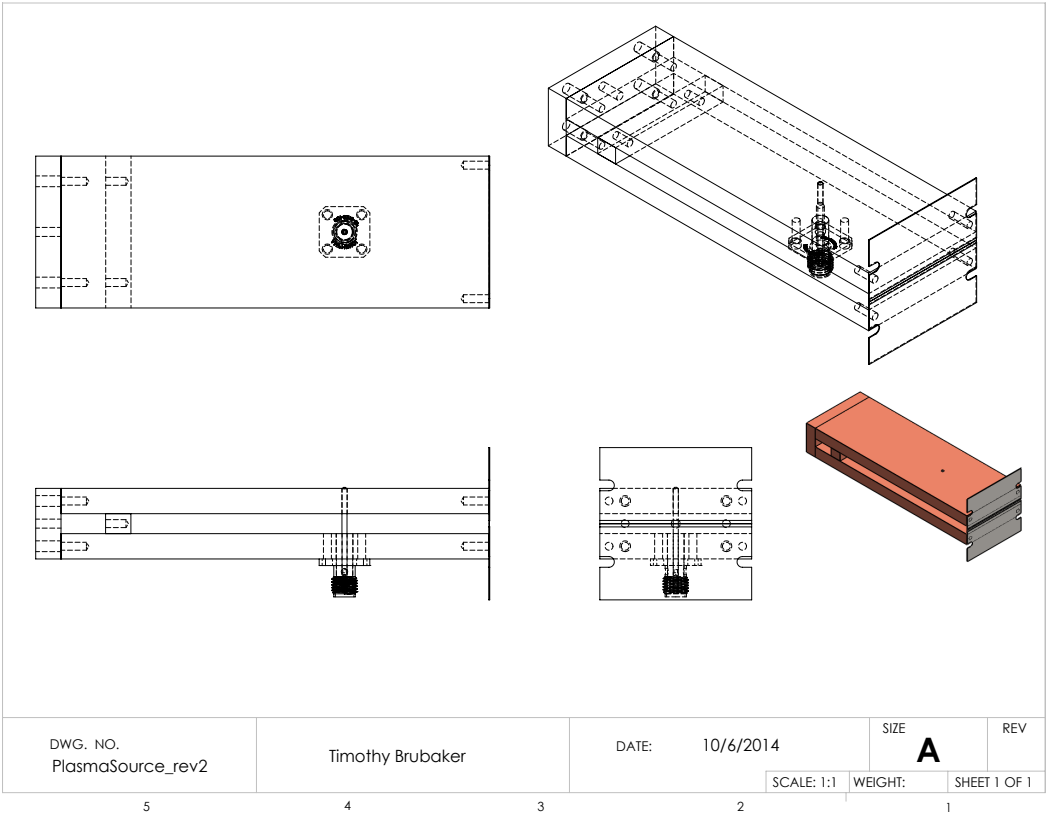


Figure B.5: Assembled plasma source.

Appendix C |

LabVIEW VI for Data Acquisition

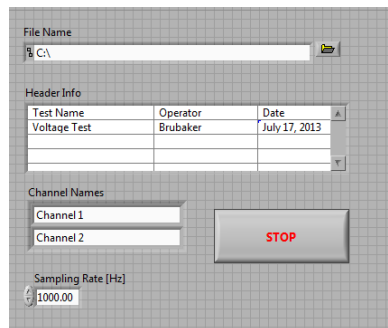


Figure C.1: Front panel of data acquisition VI.

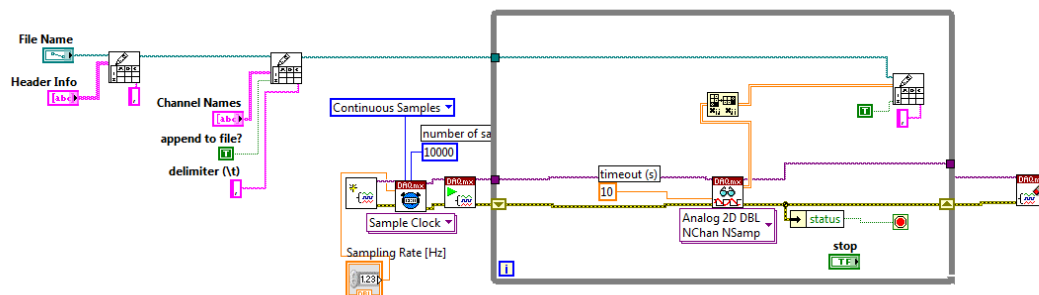


Figure C.2: Block diagram of data acquisition VI.

Appendix D |

LTS Calculator

Laser Thomson Scattering Calculator
 Created by Timothy R. Brubaker
 Calculations based on "Principles of Plasma Diagnostics", 2nd edition, by J.H. Hutchinson

Experimental Parameter:	Value	Units
Laser pulse energy, E_p	5.00E-3 J	
Wavelength, λ	532.00E-9 m	
Duration, Δt	30.00E-9 s	
Scattering Angle, θ	90.00E+0 deg (°)	
Laser beam diameter, d_{laser}	50.00E-6 m	
Scattering length, L	250.00E-6 m	
Collection optics aperture diameter, d_{col}	100.00E-3 m	
Optics distance from scattering volume, L_{col}	300.00E-3 m	
Optical transmission efficiency, Q_{opt}	500.00E-3	
Detector quantum efficiency, Q_{det}	200.00E-3	
Electron density, n_e	100.00E+18 m ⁻³	
Electron temperature, T_e	10.00E+6 eV	
Effective ion charge, Z_{eff}	116.00E+3 K	
Diameter along viewing chord	1.00E+0 n/a	
100.00E-3 m		

Constants	Value	Units
Free space Permittivity (ϵ_0)	8.85E-12 C ² /V ² m ⁻¹	
Unit charge, e (q)	1.6020E-21 C	
Boltzmann Constant, k_B	13.81E-24 m ² /kg ⁻¹ s ⁻² K ⁻¹	
pi	3.14E+0 n/a	
Classical electron radius, r_e	2.82E-15 m	
Plancks constant, h	663.00E-36	
Speed of light, c	298.00E+6 m/s	
Reciprocal of Euler's constant, ζ	1.78E+0 n/a	
mass of electron	910.90E-33 kg	

Derived Parameter	Value	Units	Comments
Debye Length, $\lambda_D = \sqrt{\epsilon_0 k_B T_e / (e^2 n_e)}$	2.35E-6 m		
Scattering regime, $k \lambda_D$	27.77E+0		Incoherent
Number of incident photons, $N_i = \lambda E_p / h c$	13.46E+15		
Collection optics solid angle, $\Omega_{col} = \pi d_{col}^2 / (4 L_{col}^2)$	87.27E-3 sr		
Number of Scattered photons at 90°, $N_s = N_i \zeta^2 \lambda_D^2 n_e L$	233.23E+0		Sets detector sensitivity
Thermal velocity of electrons, $v_{ther} = \sqrt{k_B T_e / m_e}$	1.33E+6 m/s		
Spectral width of scattered signal (down e^2), $\Delta \nu = 2 n_e v_{ther} \sin(\theta/2) / c$	4.24E+12 Hz		
	8.06E-9 m		Sets detector range
Free-free Gaunt factor, $g_{ff} = \sqrt{3} \ln(1/\ln(1/47 \sqrt{v_{ther}}))$ (LF Born approx.)	1.27E+0		
Bremsstrahlung factor, $C = 1 \times 10^{-43} g_{ff}^2$	1.27E-63		
Ratio of scattered to Bremsstrahlung photons in spectral width, $q = N_s / (N_{ff} \lambda_{col} v_{ther} / \Delta \nu \sin(\theta/2) \sin(\theta) k_B \lambda_{col} n_e Z_{eff}^2 C)$	232.32E+0		If collection time = pulse time
SNR = $(N_s / C \sin(\theta/2) \sin(\theta))^{1/2} \zeta^{-1} n_e [Q_{col} / (d_{laser} \lambda_{col})]^{1/2} T_e^{-1/2} Q_{det}^{1/2} Z_{eff}^{1/2}$	8.45E+3		If collection time = pulse time
SNR, line radiation included (factor of 500 per Sheffield 1975)	39.27E+0 dB		Bremsstrahlung radiation only
	16.90E+0		If collection time = pulse time
	12.28E+0 dB		
SNR, line radiation included (factor of 500 per Sheffield 1975)	371.38E+1 J		
Average energy per scattered photon, $E_s = h \nu_s$	86.62E-18		
Signal power at detector, $P_{det} = E_s N_s$			

Figure D.1: Excel calculator for finding LTS system SNR based on instrumentation and plasma parameters.

Bibliography

- [1] K. H. Becker, K. H. Schoenbach, and J. G. Eden, “Microplasmas and applications,” *Journal of Physics D: Applied Physics*, vol. 39, no. 3, pp. R55–R70, Feb. 2006.
- [2] K. L. Rakness, *Ozone in drinking water treatment: Process design, operation, and optimization*, 1st ed. Denver, CO: American Water Works Association, 2005.
- [3] F. Iza and J. Hopwood, “Low-power microwave plasma source based on a microstrip split-ring resonator,” *IEEE Transactions on Plasma Science*, vol. 31, no. 4, pp. 782–787, 2003.
- [4] —, “Rotational, vibrational, and excitation temperatures of a microwave-frequency microplasma,” *IEEE Transactions on Plasma Science*, vol. 32, no. 2, pp. 498–504, 2004.
- [5] —, “Split-ring resonator microplasma: Microwave model, plasma impedance and power efficiency,” *Plasma Sources Science and Technology*, vol. 14, no. 2, pp. 397–406, May 2005.
- [6] J. Hopwood, F. Iza, S. Coy, and D. B. Fenner, “A microfabricated atmospheric-pressure microplasma source operating in air,” *Journal of Physics D: Applied Physics*, vol. 38, no. 11, pp. 1698–1703, Jun. 2005.
- [7] X.-M. Zhu, W.-C. Chen, and Y.-K. Pu, “Gas temperature, electron density and electron temperature measurement in a microwave excited microplasma,” *Journal of Physics D: Applied Physics*, vol. 41, no. 10, p. 105212, May 2008.
- [8] J. Choi, F. Iza, H. J. Do, J. K. Lee, and M. H. Cho, “Microwave-excited atmospheric-pressure microplasmas based on a coaxial transmission line resonator,” *Plasma Sources Science and Technology*, vol. 18, no. 2, p. 025029, May 2009.
- [9] J. Kim and K. Terashima, “2.45 GHz microwave-excited atmospheric pressure air microplasmas based on microstrip technology,” *Applied Physics Letters*, vol. 86, no. 19, p. 191504, 2005.
- [10] A. Kono, T. Sugiyama, T. Goto, H. Furuhashi, and Y. Uchida, “Production of CW high-density non-equilibrium plasma in the atmosphere using microgap discharge excited by microwave,” *Japan Society of Applied Physics*, vol. 40, no. 3, pp. 238–241, 2001.
- [11] J. Gregorio and O. Leroy, “Design of a microwave microplasma source at atmospheric pressure,” *IEEE Transactions on Plasma Science*, vol. 37, no. 6, pp. 797–808, 2009.
- [12] C. Tendero, C. Tixier, P. Tristant, J. Desmaison, and P. Leprince, “Atmospheric pressure plasmas: A review,” *Spectrochimica Acta Part B: Atomic Spectroscopy*, vol. 61, no. 1, pp. 2–30, Jan. 2006.

- [13] A. Kono, T. Shibata, and M. Aramaki, "Heat transport simulation for atmospheric-pressure high-density microgap plasma," *Japanese Journal of Applied Physics*, vol. 45, no. 2A, pp. 940–945, Feb. 2006.
- [14] J. Waskoenig, D. O'Connell, V. Schulz- von der Gathen, J. Winter, S.-J. Park, and J. G. Eden, "Spatial dynamics of the light emission from a microplasma array," *Applied Physics Letters*, vol. 92, no. 10, p. 101503, 2008.
- [15] M. Malik, A. Ghaffar, and S. Malik, "Water purification by electrical discharges," *Plasma Sources Science and Technology*, vol. 10, no. 1, pp. 82–91, Feb. 2001.
- [16] M. B. Chang and S.-J. Wu, "Experimental study on ozone synthesis via dielectric barrier discharges," *Ozone: Science & Engineering*, vol. 19, no. 3, pp. 241–254, Jan. 1997.
- [17] M. Boeniger, "Use of ozone generating devices to improve indoor air quality," *American Industrial Hygiene Association*, vol. 56, pp. 590–598, 1995.
- [18] C. Weschler, M. Brauer, and P. Koutrakis, "Indoor ozone and nitrogen dioxide: A potential pathway to the generation of nitrate radicals, dinitrogen pentoxide, and nitric acid indoors," *Environmental Science & Technology*, vol. 26, no. 1, pp. 179–184, 1992.
- [19] C. Weschler, "Indoor chemistry: Ozone, volatile organic compounds, and carpets," *Environmental Science & Technology*, vol. 26, no. 1, pp. 2371–2377, 1992.
- [20] C. J. Weschler and H. C. Shields, "Production of the hydroxyl radical in indoor air," *Environmental Science & Technology*, vol. 30, no. 11, pp. 3250–3258, Jan. 1996.
- [21] J. Zhang and P. J. Lioy, "Ozone in residential air: Concentrations, I/O ratios, indoor chemistry, and exposures," *Indoor Air*, vol. 4, no. 2, pp. 95–105, Jun. 1994.
- [22] M. Laroussi, M. Kong, G. Morfill, and W. Stolz, *Plasma medicine: Applications of low-temperature gas plasmas in medicine and biology*. Cambridge University Press, 2012.
- [23] N. K. Kaushik, P. Attri, N. Kaushik, and E. H. Choi, "A preliminary study of the effect of DBD plasma and osmolytes on T98G brain cancer and HEK non-malignant cells," *Molecules*, vol. 18, no. 5, pp. 4917–28, Jan. 2013.
- [24] R. X. Wang, W. F. Nian, H. Y. Wu, H. Q. Feng, K. Zhang, J. Zhang, W. D. Zhu, K. H. Becker, and J. Fang, "Atmospheric-pressure cold plasma treatment of contaminated fresh fruit and vegetable slices: Inactivation and physiochemical properties evaluation," *The European Physical Journal D*, vol. 66, no. 10, p. 276, Oct. 2012.
- [25] C. Leclaire, E. Lecoq, G. Orial, F. Clement, and F. Bousta, "Fungal decontamination by cold plasma: an innovating process for wood treatment," 2008, cOST Action IE0601.
- [26] S. U. Kalghatgi, G. Fridman, A. Fridman, G. Friedman, and A. M. Clyne, "Non-thermal dielectric barrier discharge plasma treatment of endothelial cells," *International Conference of the IEEE Engineering in Medicine and Biology Society*, vol. 2008, pp. 3578–81, Jan. 2008.
- [27] S. Kalghatgi, G. Friedman, A. Fridman, and A. M. Clyne, "Endothelial cell proliferation is enhanced by low dose non-thermal plasma through fibroblast growth factor-2 release," *Annals of biomedical engineering*, vol. 38, no. 3, pp. 748–57, Mar. 2010.
- [28] M. Leduc, D. Guay, S. Coulombe, and R. L. Leask, "Effects of non-thermal plasmas on DNA and mammalian cells," *Plasma Processes and Polymers*, vol. 7, no. 11, pp. 899–909, Nov. 2010.

- [29] Y. Lee, K. Kim, K.-T. Kang, J.-S. Lee, S. S. Yang, and W.-H. Chung, "Atmospheric-pressure plasma jet induces DNA double-strand breaks that require a Rad51-mediated homologous recombination for repair in *Saccharomyces cerevisiae*," *Archives of biochemistry and biophysics*, vol. 560, pp. 1–9, Jul. 2014.
- [30] A. Semnani, A. Venkatraman, A. A. Alexeenko, and D. Peroulis, "Pre-breakdown evaluation of gas discharge mechanisms in microgaps," *Applied Physics Letters*, vol. 102, no. 17, p. 174102, 2013.
- [31] N. Braithwaite, "Introduction to gas discharges," *Plasma Sources Science and Technology*, vol. 9, pp. 517–527, 2000.
- [32] J. Cooley, "Fundamentals of undervoltage breakdown," Dissertation, Princeton University, 2008.
- [33] F. Paschen, "Ueber die zum funkenbergang in luft, wasserstoff und kohleneure bei verschiedenen drucken erforderliche potentialdifferenz," *Annalen der Physik*, vol. 37, pp. 69–96, 1889.
- [34] E. Sorolla and M. Mattes, "Corona discharge in microwave devices: A comparison of ionization rate models," *IEEE Microwave Review*, pp. 41–46, 2010.
- [35] J. T. Mayhan, "Comparison of various microwave breakdown prediction models," *Journal of Applied Physics*, vol. 42, no. 13, p. 5362, 1971.
- [36] L. Gould and L. W. Roberts, "Breakdown of air at microwave frequencies," *Journal of Applied Physics*, vol. 27, no. 10, p. 1162, 1956.
- [37] W. Scharfman, "Breakdown limitations on the transmission of microwave power through the atmosphere," *IEEE Transactions on Antennas and Propagation*, no. 69, pp. 447–455, 1964.
- [38] A. D. MacDonald, D. U. Gaskell, and H. N. Gitterman, "Microwave breakdown in air, oxygen, and nitrogen," *Phys. Rev.*, vol. 130, pp. 1841–1850, Jun 1963.
- [39] A. Semnani, A. Venkatraman, A. a. Alexeenko, and D. Peroulis, "Frequency response of atmospheric pressure gas breakdown in micro/nanogaps," *Applied Physics Letters*, vol. 103, no. 6, p. 063102, 2013.
- [40] Y. Ogino and N. Ohnishi, "A collisional-radiative code for computing air plasma in high enthalpy flow," *Shock Waves*, vol. 21, no. 3, pp. 289–299, Jun. 2011.
- [41] F. J. Gordillo-Vázquez, "Air plasma kinetics under the influence of sprites," *Journal of Physics D: Applied Physics*, vol. 41, no. 23, p. 234016, Dec. 2008.
- [42] J. Kitayama and M. Kuzumoto, "Analysis of ozone generation from air in silent discharge," *Journal of Physics D: Applied Physics*, vol. 32, no. 23, pp. 3032–3040, Dec. 1999.
- [43] S. Pekárek, "Non-thermal plasma ozone generation," *Acta Polytechnica*, vol. 43, no. 6, 2003.
- [44] U. Kogelschatz, B. Eliasson, and M. Hirth, "Ozone generation from oxygen and air: Discharge physics and reaction mechanisms," *Ozone: Science & Engineering*, vol. 10, pp. 367–378, 1988.

- [45] N. Mason, J. Skalny, and S. Hadj-Ziane, "Experimental investigations and modelling studies of ozone producing corona discharges," *Czechoslovak Journal of Physics*, vol. 52, no. 1, pp. 85–94, 2002.
- [46] R. S. Mangina, J. M. Ajello, R. A. West, and D. Dziczek, "High-resolution electron-impact emission spectra and vibrational emission cross sections from 3303–1100 nm for N₂," *The Astrophysical Journal Supplement Series*, vol. 196, no. 1, p. 13, Sep. 2011.
- [47] A. Lofthus and P. Krupenie, "The spectrum of molecular Nitrogen," *Physical Chemistry Reference Data*, vol. 6, no. 1, pp. 113–307, 1977.
- [48] Atomic Collisions Group (University of Wisconsin), "N₂ Energy Level Diagram," 2012.
- [49] M. Bazavan and I. Iova, "Temperature determination of a cold N₂ discharge plasma by the fit of the experimental spectra," *Romanian Reports in Physics*, vol. 60, no. 3, pp. 671–678, 2008.
- [50] A. Kiliánová, P. Veis, C. Foissac, C. Dupret, and P. Supiot, "Spectroscopic characterization of Nitrogen – Argon discharge created by helical cavity experimental set-up," in *WDS'07 Proceedings of Contributed Papers, Part II*, Prague, 2007, pp. 175–180.
- [51] D. Phillips, "Determination of gas temperature from unresolved bands in the spectrum from a nitrogen discharge," *Journal of Physics D: Applied Physics*, vol. 507, 1976.
- [52] M. Simek and S. De Benedictis, "On the use of the numerical simulation of the First Positive System of N₂: II. Fast trot estimation from the partially resolved (3,0) band," *Plasma Chemistry and Plasma Processing*, vol. 15, no. 3, pp. 451–463, 1995.
- [53] N. Masoud, K. Martus, M. Figus, and K. Becker, "Rotational and vibrational temperature measurements in a high-pressure cylindrical dielectric barrier discharge (C-DBD)," *Contributions to Plasma Physics*, vol. 45, no. 1, pp. 32–39, Feb. 2005.
- [54] X.-M. Zhu and Y.-K. Pu, "Optical emission spectroscopy in low-temperature plasmas containing argon and nitrogen: determination of the electron temperature and density by the line-ratio method," *Journal of Physics D: Applied Physics*, vol. 43, no. 40, p. 403001, Oct. 2010.
- [55] M. Naidu and N. Kamaraju, *High voltage engineering*, 2nd ed. McGraw Hill, 1995.
- [56] L. F. Berzak, S. E. Dorfman, and S. P. Smith, "Pachen's law in air and noble gases," Berkeley Lab, Tech. Rep., 2006.
- [57] S. Orfanidis, *Electromagnetic waves and antennas*. Rutgers University, 2013.
- [58] H. Wheeler, "Transmission-line properties of parallel strips separated by a dielectric sheet," *IEEE Transactions on Microwave Theory and Techniques*, vol. 13, no. 2, pp. 172–185, 1965.
- [59] A. International, Ed., *ASM handbook volume 1: Properties and selection: Irons, steels, and high-performance alloys*, 10th ed., 1990.
- [60] K. Shimizu, "Study of air pollution control by using micro plasma filter," *IEEE Transactions on Industry Applications*, vol. 44, no. 2, pp. 506–511, 2008.
- [61] I. H. Hutchinson, *Principles of plasma diagnostics*, 2nd ed. Cambridge University Press, 2005.

- [62] S. Hübner, J. S. Sousa, V. Puech, G. M. W. Kroesen, and N. Sadeghi, “Electron properties in an atmospheric helium plasma jet determined by Thomson scattering,” *Journal of Physics D: Applied Physics*, vol. 47, no. 43, p. 432001, Oct. 2014.
- [63] A. V. Lammeren, C. Barth, Q. van Est, and F. Schuller, “Non-maxwellian electron velocity distributions observed with thomson scattering in the tortur tokamak,” *Nuclear Fusion*, vol. 32, no. 4, p. 655, 1992.
- [64] I. Pastor, J. Guasp, R. Álvarez-Estrada, and F. Castejón, “Numerical computation of thomson scattering spectra for non-maxwellian or anisotropic electron distribution functions,” *Nuclear Fusion*, vol. 52, no. 12, p. 123013, 2012.
- [65] F. Box, “Non-maxwellian thomson scattering spectra at the rtp tokamak as a new diagnostic tool,” *Nuclear Fusion*, vol. 39, no. 9, p. 1193, 1999.